Materials Today Physics 28 (2022) 100883

Contents lists available at ScienceDirect

Materials Today Physics

journal homepage: www.journals.elsevier.com/materials-today-physics

Review of self-powered solar-blind photodetectors based on Ga_2O_3

Chao Wu, Fengmin Wu, Haizheng Hu, Shunli Wang, Aiping Liu, Daoyou Guo *

Department of Physics, Zhejiang Sci-Tech University, Hangzhou, 310018, China

ARTICLE INFO

Keywords:
Ga_2O_3
Solar-blind
Self-powered
Photodetector

ABSTRACT

Due to the broad potential applications range in both military and civilian domains, solar-blind photodetectors based on the ultrawide-bandgap semiconductor Ga_2O_3, with high photosensitivity and low false alarm rate, have been widely concerned. With the rapid development of modern society, photodetectors are gradually being modified to exhibit high energy efficiency, miniaturization, and excellent performance. Self-powered photodetectors based on the photovoltaic effect can detect optical signals without an external power source, emerging as a promising candidate for next-generation photodetectors. This review summarizes the state-of-the-art research on self-powered solar-blind photodetectors based on Ga_2O_3. We classify the currently reported Ga_2O_3-based self-powered solar-blind photodetectors into Schottky junction (including metal-semiconductor and graphene-semiconductor types), heterojunction (including all-inorganic and inorganic-organic types), phase junction, and photoelectrochemical (PEC). The fundamental properties of Ga_2O_3, the basic working principles of self-powered photodetectors, and the device processing developments have been summarized. Finally, conclusions regarding recent advances, remaining challenges, and prospects are presented and discussed.

1. Introduction

The ultraviolet (UV) light released by the sun is typically classified as ultraviolet A (UVA) spectrum (320–400 nm), ultraviolet B (UVB) spectrum (280–320 nm), ultraviolet C (UVC) spectrum (100–280 nm), and extreme ultraviolet (EUV) spectrum (10–120 nm) [1]. The UV spectrum between 200 and 280 nm has a low background level on the surface of the planet because almost all of it is absorbed by the atmosphere. As a result, this region is known as the solar-blind region [2]. The function of a solar-blind photodetector is to convert solar-blind light intensity information into a measurable electrical signal. With a wide range of military and civilian uses, recent breakthroughs in solar-blind photodetectors with high photosensitivity and low false alarm rates have raised great attentions.

Photomultiplier tubes (PMTs), thermal detectors, narrow bandgap semiconductor photodiodes, and charged-coupled devices (CCD) have traditionally been used to detect solar-blind light. PMTs are blind to photons that have wavelengths longer than solar-blind, but they often call for a high voltage of more than 100 V and are bulky due to their large size and high weight, which leads to a huge amount of power consumption and an inconvenience. Thermal detectors are just as useful as absolute radiometric standards, often used for UV light calibration. However, their response is sluggish and not wavelength-dependent, making them unsuitable for quick and wavelength selective detection of solar-blind radiation. The operation of narrow bandgap semiconductor photodiodes and CCDs requires only moderate voltages, and the devices are more compact, lightweight, as well as affordable than their predecessors. However, the system's effective area is significantly decreased because of the costly optical filters required to filter out visible and infrared photons owing to the small bandgap of semiconductor semiconductors. Additionally, the inevitable aging of devices is brought on by exposure to radiation with energy much above the semiconductor's bandgap.

Ultrawide-bandgap semiconductors are considered the most effective semiconductors for solar-blind light detection since their band gaps are larger than 3.4 eV [3,4]. As one of them, Ga_2O_3 (E_g~4.9 eV) is a natural solar-blind detection material with a high breakdown electric field, high saturated electron mobility, low dielectric constant, and high thermal conductivity, which have made it a hot-spot material in the past decade. A quantity of Ga_2O_3 based high-performance solar-blind photodetectors have been fabricated by researchers worldwide, while most of them need to be powered by an external power source [5–7]. Photodetectors are gradually being improved to have the qualities of high efficiency, energy savings, and miniaturization due to the rapid rise of modern society. The self-powered photodetectors based on the photovoltaic effect have excellent performance and can detect light without an

* Corresponding author.
E-mail address: dyguo@zstu.edu.cn (D. Guo).

https://doi.org/10.1016/j.mtphys.2022.100883
Received 17 July 2022; Received in revised form 27 September 2022; Accepted 6 October 2022
Available online 20 October 2022

external power source, which makes them perfect for next-generation photodetectors. Reports of Ga_2O_3-based self-powered solar-blind photodetectors have increased year by year in the last decade. According to the charge transfer characters at the interface, the reported self-powered photodetectors can be segmented into Schottky junction, heterojunction, phase junction, and photoelectrochemical (PEC). To summarize the physical mechanisms, advanced materials, and device architectures in this field, a thorough analysis of self-powered Ga_2O_3--based solar-blind photodetectors is required.

2. Material properties of Ga_2O_3

Ga_2O_3 has been studied for a long time. The polymorphs of Ga_2O_3 and their zones of stability were established in 1952, which was the impetus for the subsequent phase of the study [8]. There are six different phases of Ga_2O_3, which are denoted by the symbols α, β, γ, ε, δ, and κ, respectively. As shown in Fig. 1, the α-Ga_2O_3 has a corundum structure with only octahedral coordination Ga sites. Thanks to the similar crystal structure to corundum-structured III-oxide materials, alloys and heterostructures can lead to various novel multifunctional devices [9–14]. β-Ga_2O_3 is monoclinic, with lattice parameters of a = 12.21 Å, b = 3.04 Å, c = 5.80 Å, and β = 103.8°, containing two crystallographically different Ga cations (tetrahedral coordination and octahedral coordination) and three types O anions [15–19]. Anisotropic distribution of the physical, optical, and electrical characteristics is produced by the monoclinic phase, which has a low level of crystallographic symmetry. γ-Ga_2O_3 belongs to a defective spinel structure with lattice parameters of 8.22 Å and the ratio of octahedral and tetrahedral coordination Ga is 2 [20–24]. It is widely believed that ε-Ga_2O_3 has an orthorhombic structure though the disordering Ga in ε-Ga_2O_3 makes its structure elusively [25,26]. In the current literature, κ-Ga_2O_3, which is orthorhombic and has the space group Pna21, is often mistaken for the disordered structure with P63mc space group symmetry. Among the six phases, β-Ga_2O_3 is the most stable and widely used material in solar-blind photodetectors [8].

The electrical and optical characteristics of semiconductor materials are the optoelectronic devices' primary focus. Using first-principles calculations and numerous spectral tests, researchers have thoroughly examined the electronic structure of Ga_2O_3 [27–31]. The conduction band (CB) of β-Ga_2O_3 is mainly made up of delocalized Ga 4s derived states, which makes it a dispersive band with a low electron-effective mass. On the other hand, the valence band (VB) is mainly made up of occupied O 2p6 derived states, with hybridization with Ga 3d, 4p, and 4s orbitals [30]. Due to the huge hole's effective mass and limited mobility, most doped holes tend to get trapped by local lattice structures as polarons, resulting in an extremely low p-type probability.

The essential material characteristics of the main semiconductors are compared with Ga_2O_3 in Table 1. In contrast to other wide bandgap materials like AlGaN [32,33], MgZnO [34], etc., Ga_2O_3 has an appropriate bandgap, thus, it does not need doping to modify it and prevents alloy composition fluctuations and phase separation. More importantly, 6-inch Ga_2O_3 single crystals and epitaxial films are now available owing to the development of growth technology. Research on solar-blind photodetectors based on Ga_2O_3 has been gaining momentum all around the globe, particularly after 2014, as shown in Fig. 2.

3. The general theory of self-powered photodetectors

3.1. Classifications of self-powered photodetectors

As illustrated in Fig. 3, recently reported Ga_2O_3 self-powered photodetectors may be classified into heterojunction, Schottky junction, phase junction, and PEC types.

3.1.1. Heterojunction

A statistical distribution function may be used to explain the chance that an electron would occupy an energy level (E) according to quantum statistical theory [35]:

$$f(E) = \frac{1}{1 + \exp\left(\frac{E - E_F}{KT}\right)} \tag{1}$$

where k is Boltzmann constant, E_F is Fermi energy level, and T is thermodynamic temperature. The equation states that when two semiconductors with various Fermi energy levels are combined to form a heterojunction, the valence electrons from the semiconductor with the higher E_F escaped and injected into the semiconductor with the lower E_F's empty energy state. At the heterojunction interface, this electron transfer process, which is essentially a thermal diffusion process, will produce an intrinsic electric field that simultaneously lowers the energy band of the semiconductor with higher E_F and raises the energy band of the semiconductor with lower E_F, resulting in band bending.

Ga_2O_3 heterojunctions contain nn-type and pn-type since the Ga_2O_3 is an inherently n-type semiconductor. The energy band organization and carrier transport procedures of nn-type and pn-type heterojunctions are shown in Figs. 4 and 5, respectively, where N refers to an n-type semiconductor, P refers to a p-type semiconductor, the subscript character 1 refers to semiconductor 1, the subscript character 2 refers to semiconductor 2, E_c refers to the conduction band, E_v refers to the valence band, E_F refers to the Fermi energy, χ refers to the electron affinity of the semiconductors, E_g refers to the bandgap of the semiconductors, W refers to the work function of the semiconductors, ΔE_c refers to the conduction band offset between two semiconductors, ΔEv refers to the valence band offset between two semiconductors, E_D and V_D refer to the built-in electric field and the built-in potential difference respectively.

As shown in Fig. 4(a), the CB, VB, and E_F of the semiconductor N_1 are higher than those of N_2 before contact. When N_1 comes into contact with

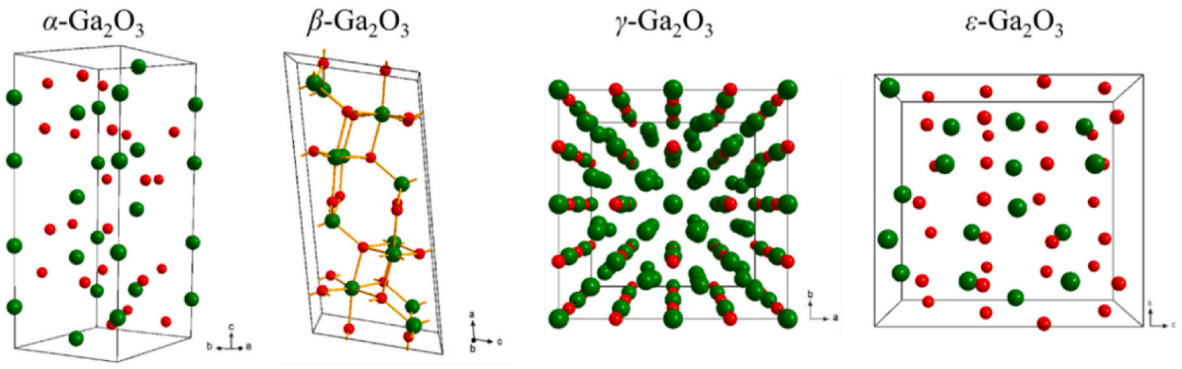

Fig. 1. Crystal structures of several polymorphs of Ga_2O_3 (Ga green, O red). (For interpretation of the references to colour in this figure legend, the reader is referred to the Web version of this article.)

Table 1
Material properties of major semiconductors and Ga_2O_3.

Parameters	Si	SiC	GaN	Ga_2O_3	Diamond	AlN
E_g (eV)	1.1	3.3	3.4	4.5–5.3	5.5	6.2
Breakdown field (MV/cm)	0.3	2.6	3.3	5–9	10	2
Electronic mobility (cm^2/V·s)	1400	1000	1200	300	2000	155
Thermal conductivity (W/cmK)	1.5	2.7	2.1	0.23 [010] 0.13 [100]	22	13
Baliga's figure of merit ($\varepsilon\mu E_b^3$)	1	340	870	3443	24 664	–
Johnson's figure of merit ($E_bV_s/\pi)^2$	1	177.6	756	1093	–	–
Substrate size (inch)	12	8	2	6	1	2
Response spectrum (nm)	400–1100	200–370	200–300	< 280	< 225	< 200

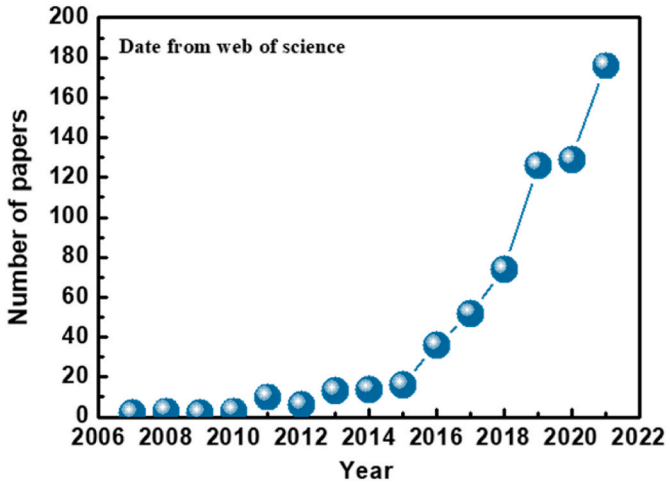

Fig. 2. Number of publications on Ga_2O_3 based photodetector from 2006 to 2022 (Data from: Web of science).

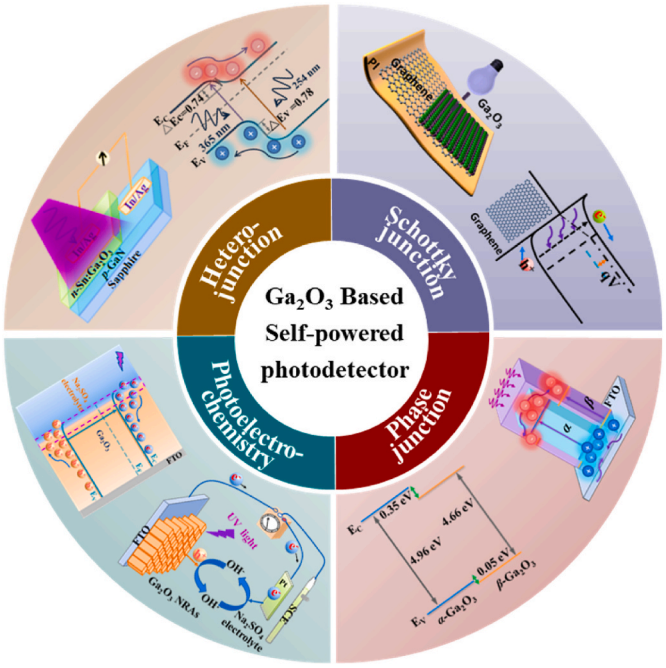

Fig. 3. Different types of Ga_2O_3 based self-powered solar-blind photodetectors.

N_2 to form an nn type heterojunction, electrons will spontaneously diffuse from the high Fermi energy level to the low Fermi energy level, which will result in the formation of positive charge centers in the interface region of N_1 and the accumulation of electrons in the interface region of N_2. As a result, a built-in electric field will form at the interface between N_1 and N_2 in the direction of N_1 to N_2. This built-in electric field will prevent continuous electron passage from N_1 to N_2 until thermal equilibrium conditions are met, as illustrated in Fig. 4(b). Under light irradiation, the photoexcited holes will be moved to the VB of N_2, whereas the photoexcited electrons will be transferred to the CB of N_1 by the effect of the built-in electric field (Fig. 4(c)).

Fig. 5 is the schematic representation of the energy-band diagrams of the pn junction. As shown in Fig. 5(a), the CB and VB of the semiconductor N are lower than those of P, while the E_F of the semiconductor N is higher than that of P before contact. When N comes into contact with P to form a pn type heterojunction, electrons will spontaneously diffuse from the high Fermi energy level to the low Fermi energy level, which will result in the formation of positive charge centers in the interface region of N and the accumulation of electrons in the interface region of P. As a result, a built-in electric field will form at the interface between N and P in the direction of N to P. This built-in electric field will prevent continuous electron passage from N to P until thermal equilibrium conditions are met, as illustrated in Fig. 5(b). Under light irradiation, the photoexcited holes will be moved to the VB of P, whereas the photoexcited electrons will be transferred to the CB of N by the effect of the built-in electric field (Fig. 5(c)).

3.1.2. Schottky junction

According to the ideal Schottky-Mott model, the difference in work functions between metal (Φ_m) and semiconductor (Φ_s) determines the contact types. For n-type Ga_2O_3, a Schottky contact will form if $\Phi_m > \Phi_s$ and the barrier height is defined as $\Phi_s = \Phi_m - \chi_s$, where χ_s is the electron affinity of the semiconductor [36,37]. Ideality factor (n) and Schottky barrier height (Φ_B) are two of the criteria parameters that affect the performances of Schottky junction-type devices. The thermionic emission theory describes carriers' transport to overcome the barrier at the metal-semiconductor interface, and the current at the interfaces can be written as follows, respectively [38–41]:

$$I = I_0\left[exp\left(\frac{qV}{nkT} - 1\right)\right] \tag{2}$$

$$I_0 = AA^*T^2\ \exp\left(-\frac{q\Phi_B}{\kappa T}\right) \tag{3}$$

where I_0 is the reverse saturation current, A is the area of the metal-semiconductor contact, A* is the effective Richardson constant, V is the bias applied to the Schottky junction device anode, n is the ideality factor, k is the Boltzmann constant, and Φ_B is the Schottky barrier height.

Fig. 6 is the schematic representation of the energy-band diagrams of

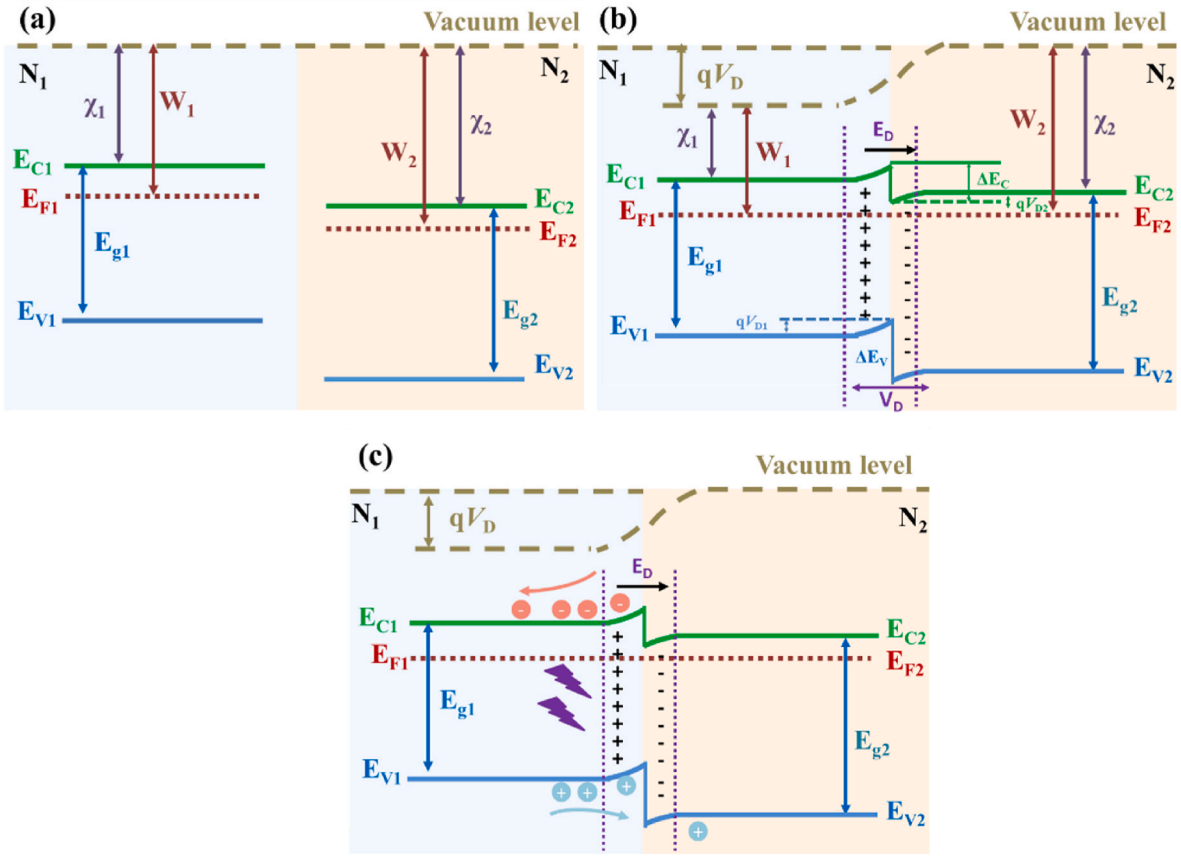

Fig. 4. Energy-band diagrams and work mechanisms of the nn type heterojunction photodetectors.

the Schottky junction. As shown in Fig. 6(a), the E_F of the semiconductor N is higher than that of metal before contact. When N comes into contact with metal to form a Schottky-type heterojunction, electrons will spontaneously diffuse from the high Fermi energy level to the low Fermi energy level, which will result in the formation of positive charge centers in the interface region of metal and the accumulation of electrons in the interface region of N. As a result, a built-in electric field will form at the interface between N and metal in the direction of N to metal. This built-in electric field will prevent continuous electron passage from N to the metal until thermal equilibrium conditions are met, as illustrated in Fig. 6(b). Under light irradiation, the photoexcited holes will be moved to the metal, whereas the photoexcited electrons will be transferred to the CB of N by the effect of the built-in electric field (Fig. 6(c)).

3.1.3. *Phase junction*

In light of the numerous polymorphs of Ga_2O_3, the scientists suggested designing a structure for self-powered solar-blind photodetectors that consists of two different polymorphs of Ga_2O_3 (phase junction). The minor lattice mismatch and similar band gap between two different polymorphs of Ga_2O_3 will improve the performances of the Ga_2O_3 based photodetectors. Since all Ga_2O_3 crystalline phases are considered to be n-type conducting, the energy band organization and carrier transport mechanisms in Ga_2O_3 crystalline phases are almost identical to those in nn-type heterojunctions.

3.1.4. *Photoelectrochemical*

Fig. 7 depicts the working process of PEC photodetectors using semiconductors as a photoanode. If the redox potential of the electrolyte is lower than the Fermi level of the semiconductor, the space charge layer will form because of the charge distribution difference between the materials and generate a built-in electric field. The photogenerated holes migrate to the semiconductor/electrolyte interface and trap an electron donor in the electrolyte, resulting in an oxidized redox species [42]. In contrast, the electrons diffuse through the semiconductor and reach the transparent conductive oxide (TCO) electrode, resulting in external circuit electrons. On the other hand, the oxidized redox species will permeate through the electrolyte and eventually reach the counter electrode. Following that, electrons at the counter electrode will decrease the oxidized redox species, completing the circuit.

3.2. *Parameters of self-powered photodetectors*

Researchers have developed a mature system to evaluate the performance of photodetectors. The significant parameters include dark current, photocurrent, and so on [43–46].

Dark current, which is the residual current that continues to flow through the photodetector even in the absence of any incident light, is primarily composed of majority drift current, tunnelling current, and generation-recombination current. The dark current of a self-powered photodetector should ideally be zero so that when exposed to light, only photogenerated carriers arise and even the smallest signals can be detected. Such ideality, however, is not attainable because there will always be some sort of dark current. Temperature, material quality, and photodetector structure all affect the dark current. The prerequisite for reducing the dark current is the use of high-quality, defect-free materials.

When a sufficient energy light illuminates at the photodetector, the light current (I_{light}) is generated. Photocurrent (I_{photo}) is calculated by subtracting light current from dark current:

$$I_{photo} = I_{light} - I_{dark} \tag{4}$$

Photo-to-dark current ratio (PDCR) can be calculated with the equation. The PDCR is also expressed as I_{photo}/I_{dark} ratio:

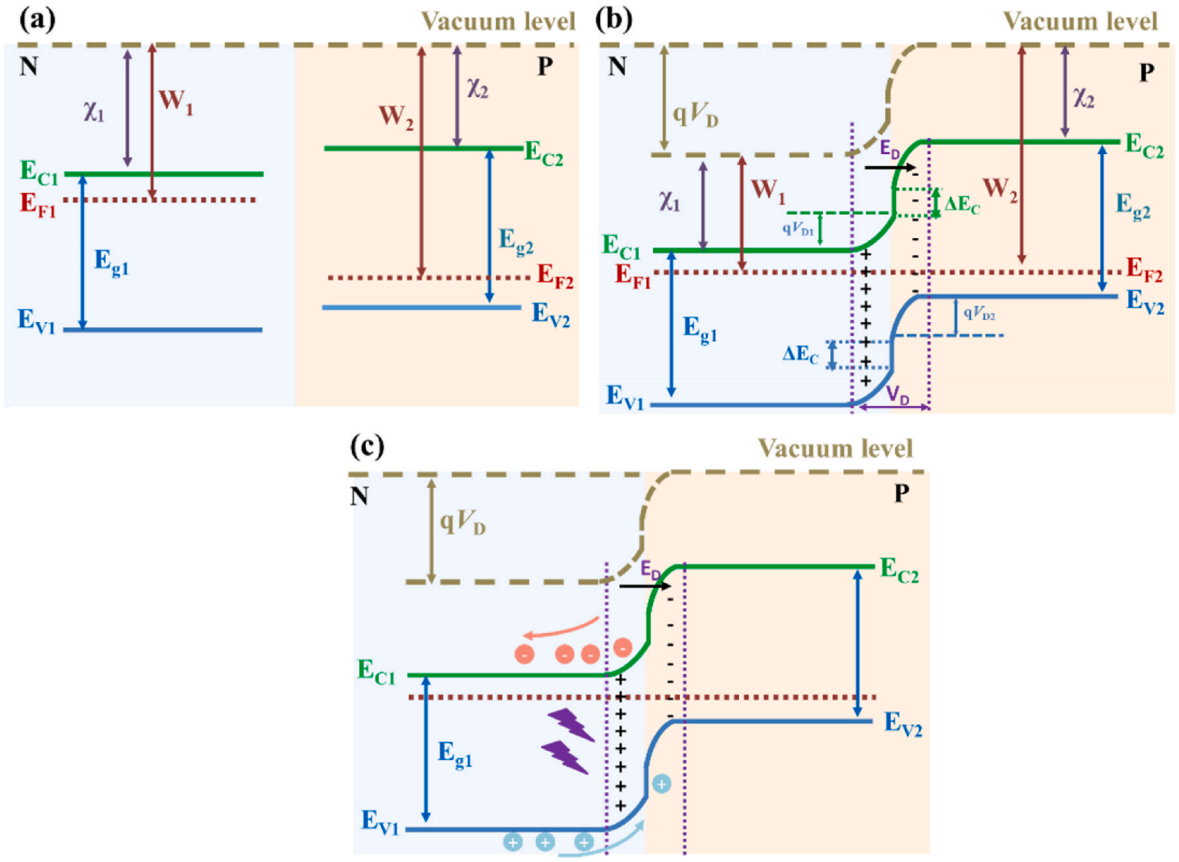

Fig. 5. Energy-band diagrams and work mechanisms of the pn type heterojunction photodetectors.

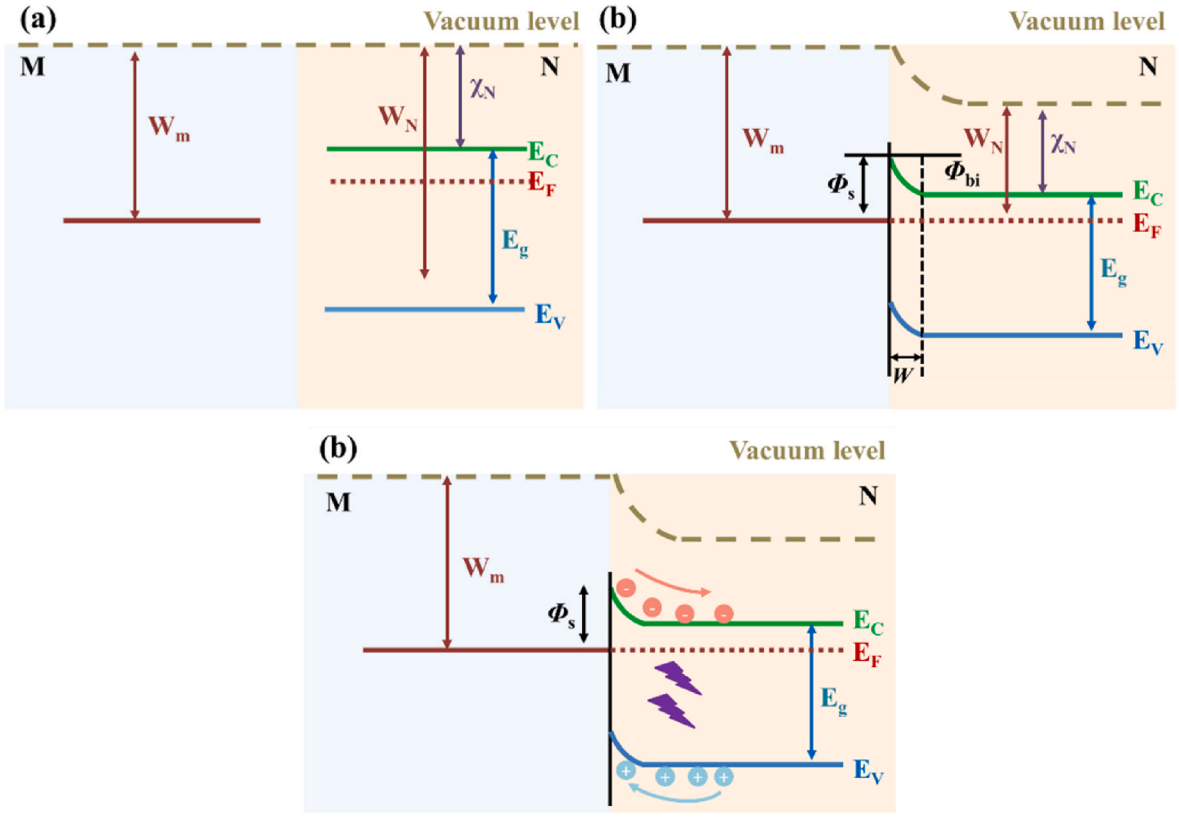

Fig. 6. Energy-band diagrams and work mechanisms of the Schottky junction type photodetectors.

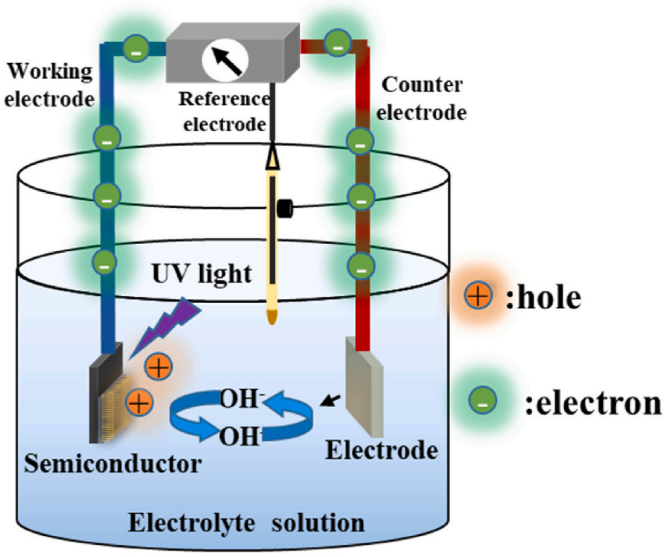

Fig. 7. Energy-band diagrams and work mechanisms of the PEC type photodetectors.

$$\mathrm{PDCR} = I_{photo} / I_{dark} \tag{5}$$

Carrier migration in the photodetector takes time which is called the response time. Response time is used to demonstrate the operating speed of the photodetector, which is calculated by fitting the photo-response curve:

$$I = I_0 + Xe^{-t/\tau_1} + Ye^{-t/\tau_2} \tag{6}$$

here I_0 is the stable state current and t is the response time, X and Y are constants, τ_1 and τ_2 are two relaxation time constants.

Responsivity (R) can be described as the photocurrent per unit of incident light intensity at a particular wavelength:

$$R = \frac{I_{photo}}{PS} \tag{7}$$

P is the light intensity, and S is the effective illuminated area.

To be effective as a solar-blind photodetector, the peak responsivity must be below 280 nm. The responsivity depends on the device structure and morphology of the material. If there are more defect states (such as in the case of amorphous or heterostructures), then the corresponding gain (and hence responsivity) is high.

Detectivity (D) is used to measure the noise of the photodetector:

$$D = \frac{R_\lambda}{\sqrt{2qI_{dark}A}} \tag{8}$$

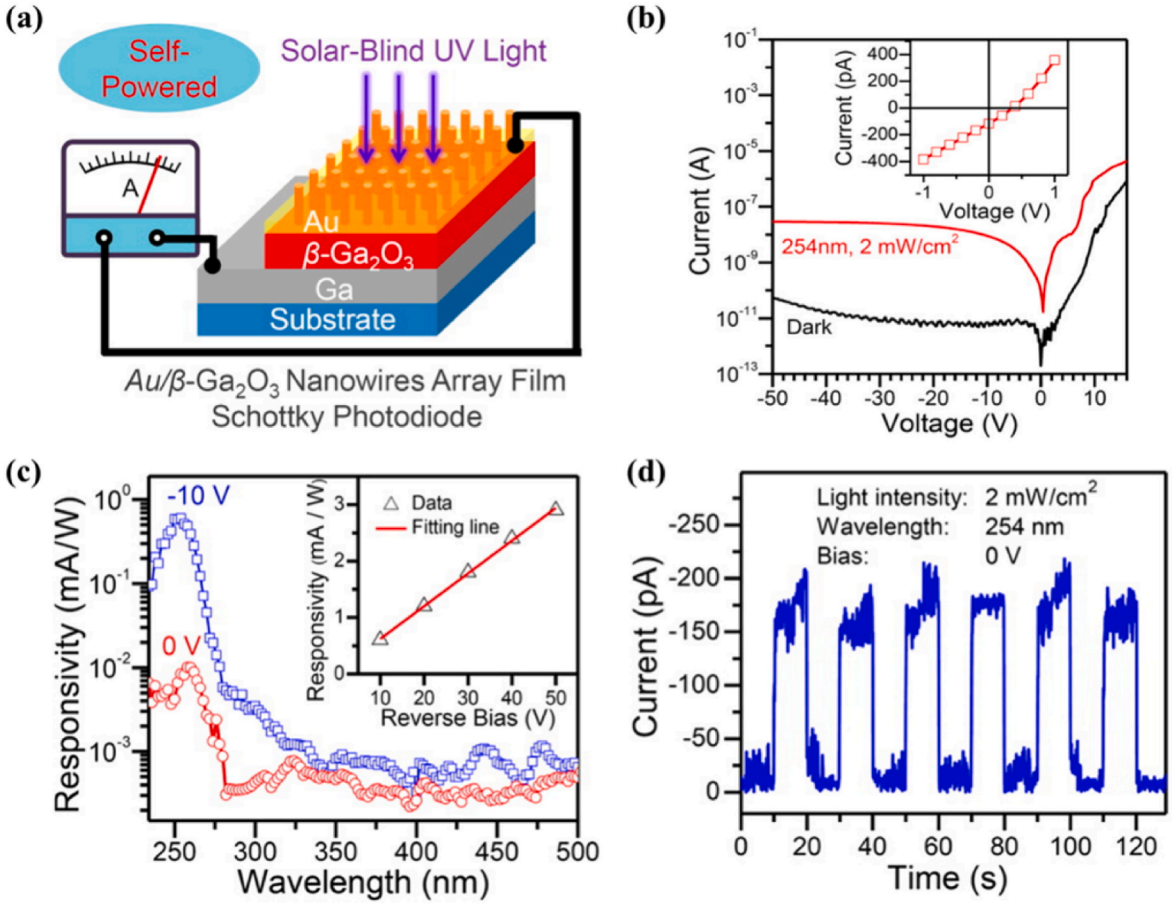

Fig. 8. (a) Device structure schematic of the vertical Au/β-Ga_2O_3 nanowires Array Schottky junction photodetector. (b) *I–V* characteristics of the device in dark and under the illumination of 254 nm light in the logarithmic scale. Inset shows the photovoltaic characteristic of the device near zero bias. (c) Spectral responses of the device at zero bias and under reverse bias of 10 V. Inset shows the responsivity of photodetectors at the wavelength of 254 nm as a function of reverse bias. (d) Time-dependent photocurrent response of Au/β-Ga_2O_3 nanowires array film Schottky junction photodetector measured at 0 V, illuminated by 254 nm light with the intensity of 2 mW/cm^2 [47].

4. Schottky junction type Ga_2O_3 based self-powered photodetectors

A semiconductor and two Ohmic contact electrodes are typical components of conventional Ga_2O_3-based photoconduction photodetectors. These photodetectors typically exhibit substantial photoconductive gain and great responsivity, but an external bias is required to separate the photoinduced electron-hole pairs. A Schottky junction type device may be created by substituting a Schottky contact electrode for an Ohmic contact electrode.

4.1. Semiconductor-metal Schottky junction

In this section, we will summarize the Ga_2O_3-based semiconductor-metal type Schottky junction self-powered photodetectors with various metals such as Pt, Ni, and Cu [44–49].

In 2016, Chen et al. designed a vertical Au/Ga_2O_3 nanowire Schottky junction photodetector (Fig. 8 (a)) [47]. The β-Ga_2O_3 nanowire arrays were synthesized by a simple thermal oxidation method, and then 20-nm Au was deposited on them to form Au/Ga_2O_3 nanowire Schottky junction photodetector. The photodetector shows a typical photovoltaic effect *I–V* curve with an open-circuit photovoltage of 0.36 V (Fig. 8(b)). As shown in Fig. 8(c), the Au/Ga_2O_3 nanowire Schottky junction photodetector exhibits the peak responsively about 0.01 mA/W at 0 V, exhibiting the characteristics of the self-powered. Meanwhile, the photodetector exhibits a solar-blind spectral selectivity with a solar-blind/UV ($R_{258\ nm}/R_{280\ nm}$) rejection ratio of 11.

Compared with nano-structure material, bulk and thin film have the advantages of uniformity, large-scale production, and integration. In 2018, Yang and his co-workers built a simple self-powered Schottky junction photodetector by depositing an Au electrode on the β-Ga_2O_3 crystal (Fig. 9 (a)) [48]. At zero bias, the photodetector shows a high spectral selectivity with $R_{256\ nm}/R_{280\ nm}$ and $R_{256\ nm}/R_{400\ nm}$ rejection ratios of 280 and 1080, respectively (Fig. 9 (b) and (c)). In 2017, Fikadu Alema et al. grew a Ga_2O_3:Ge film on (010) oriented Sn doped Ga_2O_3 substrates by plasma-assisted molecular beam epitaxy (plasma-assisted MBE) [49]. Subsequently, Pt (30 nm)/Ni(100 nm)/Pt (20 nm) electrode and Ni(20 nm)/Al (100 nm)/Ni(50 nm) metal stack layers were

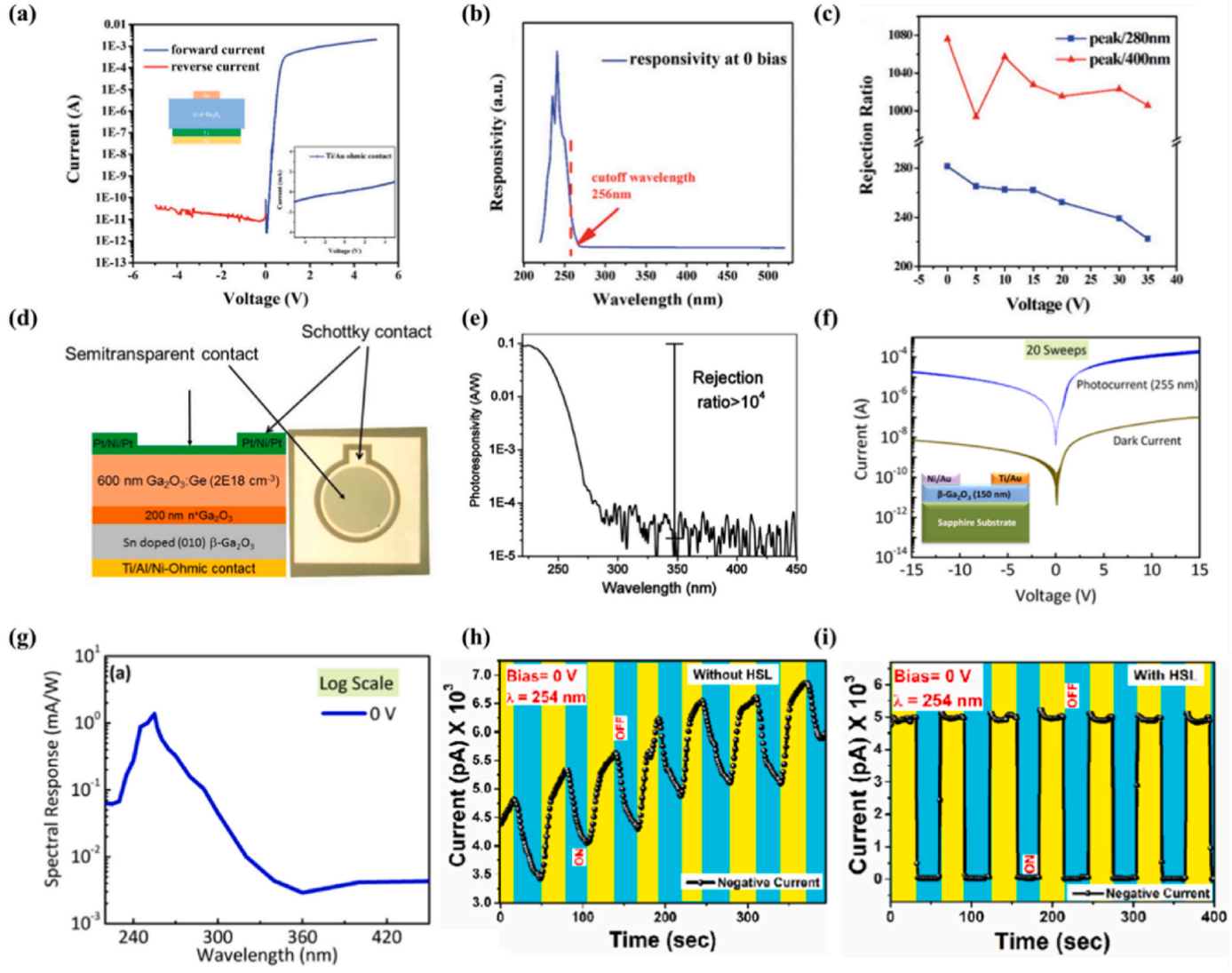

Fig. 9. (a) *I–V* characteristics of the Au/Ga_2O_3 solar-blind photodetector at dark condition. The inset depicts the Ohmic contact characterize on the bottom side of the single crystal Ga_2O_3. Photoresponse characteristics for this photodetector are shown in (b) Responsivity at 0 bias, and (c) solar-blind/visible and solar-blind/UV rejection ratio at different bias [48]. (d) Cross-sectional view of the photodetector based on Ga_2O_3:Ge homoepitaxial film grown on the bulk n^+ Ga_2O_3 substrate and optical image of the top view of the vertical Schottky junction. (e) Spectral response of the Pt–Ga_2O_3:Ge vertical Schottky junction [49]. (f) Photo and dark *I–V* characteristics at room temperature for the Ni/Au/β-Ga_2O_3 photodetector. (g) Spectral response versus wavelength at zero bias in log scale (self-powered) corresponding to EQE of 0.5% [50]. (h) and (i) Time-dependent photoresponse of β-Ga_2O_3 thin film deposited without and with HSL, respectively [51].

evaporated on the Ga_2O_3 film to form Schottky and Ohmic contact electrodes, respectively (Fig. 9(d)). The Pt/Ga_2O_3:Ge/n^+-Ga_2O_3 (010) Schottky junction photodetector shows a maximum responsivity of about 0.09 A/W at 0 V (Fig. 9(e)). The solar-blind/UVA rejection ratio ($R_{230\ nm}/R_{350\ nm}$) of the device exceeds four orders of magnitude, which indicates the excellent selectivity of the photodetector (Fig. 9(e)). Inspired by the above study, in 2018, Pratiyush et al. used Ni/Au electrode to create a Schottky junction photodetector (Fig. 9(f)) [50]. Thanks to the large barrier height and built-in electric field at the Ni/Au/Ga_2O_3 junction, the device exhibits a spectral responsivity of 1.4 mA/W at 255 nm with a response time of 1.1 s/0.3 s and a PDCR of about 10^3 at 0 V (Fig. 9(g)). To promote the industrialization of the Ga_2O_3--based Schottky junction photodetector, Ga_2O_3 needs to be prepared on regular Si-substrates. However, the large lattice and thermal expansion coefficient mismatch between Si and Ga_2O_3 degrades the device's performance. Arora et al. [51] grew highly crystalline β-Ga_2O_3 films on silicon substrates using RF magnetron sputtering and high-temperature seed layers (HSL). HSL plays an essential role in the growth of highly crystalline Ga_2O_3 films, and the photodetector without HSL shows a constant photoconductivity effect (PPC) and large dark currents, while the photodetector with HSL shows a fast response speed and low dark current (Fig. 9(i)).

One of the major drawbacks of the conventional Schottky type solar-blind photodetectors is the small photo-detectable effective area. To solve the problem, in 2020, Xu et al. used an edge-defined film fed method to grow a lager square-shape (7 mm × 7 mm) unintentional doped β-Ga_2O_3 crystal, then deposited Ti/Au and Au metal on the opposite via electron beam evaporation to form a Schottky junction photodetector (Fig. 10(a)) [52]. The photodetector exhibits a maximum responsivity value of 9.78 A/W at 212 nm, a high solar-blind to UVA rejection ratio of about 10^4, and a specific detectivity of 3.92×10^{14} Jones at 0 V. Thanks to the low dislocation density ($< 10^4$ cm^{-2}) of the crystal, the photodetector exhibits a super-fast response speed of about 5 μs (Fig. 10(b)). Recently, laser-induced graphene (LIG) electrodes were used to form Schottky contact with Ga_2O_3 [53]. Laser-induced graphene (LIG) is a straightforward, eco-friendly, cost-effective, and mask-free process for creating different forms on a flexible substrate in situ. By controlling the work function of LIG, a self-powered photodetector with a PDCR of about 200 and excellent mechanical flexibility was obtained (Fig. 10(c) and (d)).

4.2. Semiconductor-graphene Schottky junction

Although semiconductor-metal Schottky junction photodetector has many advantages, the strong light absorption and reflection of traditional film-type metal upper electrodes weakened its detection performance. To solve this problem, transparent and conductive graphene electrodes have been proposed as a substitute [54]. Due to its greater work function of graphene (~4.6 eV) than the n-doped Ga_2O_3 (~4.0 eV), graphene forms a Schottky contact with Ga_2O_3. Meanwhile, a monolayer graphene film exhibits about 95% transmittance at the solar-blind region with hole mobility as high as 8800 $cm^2/V{\cdot}S$[55,56]. In 2018, Kalita et al. transferred a monolayer graphene on the Sn-doped β-Ga_2O_3 crystal to build a Schottky junction solar-blind photodetector (Fig. 11(a)) [57]. The photodetector shows a response time of 0.62/0.67 s at a zero bias (Fig. 11(b) and (c)). In 2019, Chen et al. prepared a solar-blind graphene/β-Ga_2O_3 Schottky junction photodetector by transferring a monolayer graphene onto the β-Ga_2O_3 crystal (Fig. 11(d)) [58]. The photodetector exhibits a fast response time of 2.24 μs and a responsivity of 10.3 mA/W at 0 V. The fast response and high sensitivity can be attributed to the high mobility of the graphene electrode's and the low defect density of the β-Ga_2O_3 film (Fig. 11(e)).

The Ga_2O_3-graphene Schottky junction photodetector can operate in photovoltaic mode, while most reported Schottky junction photodetectors operate under bias to perform well. For example, Ai et al. reported a graphene/β-Ga_2O_3 Schottky junction photodetector (Fig. 12(a)) [59]. At 10 V bias, the photodetector shows a photocurrent ratio of 88.28 (I_{254}/I_{dark}) with a responsivity of 9.66 A/W (Fig. 12(b)). Kong et al.

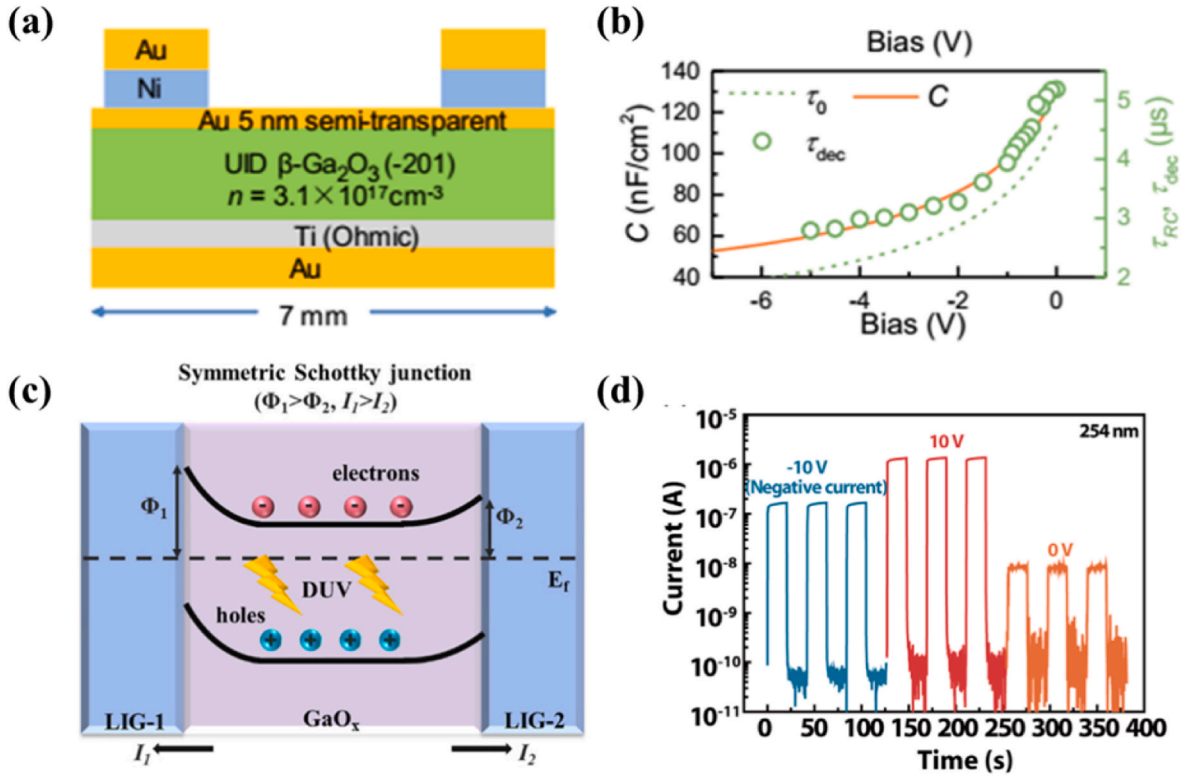

Fig. 10. (a) Cross-section schematic of the vertical β-Ga_2O_3 Schottky junction photodetector. (b) Response decay time and capacitance as a function of reverse bias [52]. (c) Schematic diagram of the self-powered LIG/Ga_2O_3 photodetector. (d) *I-t* curve of the LIG/Ga_2O_3 photodetector [53].

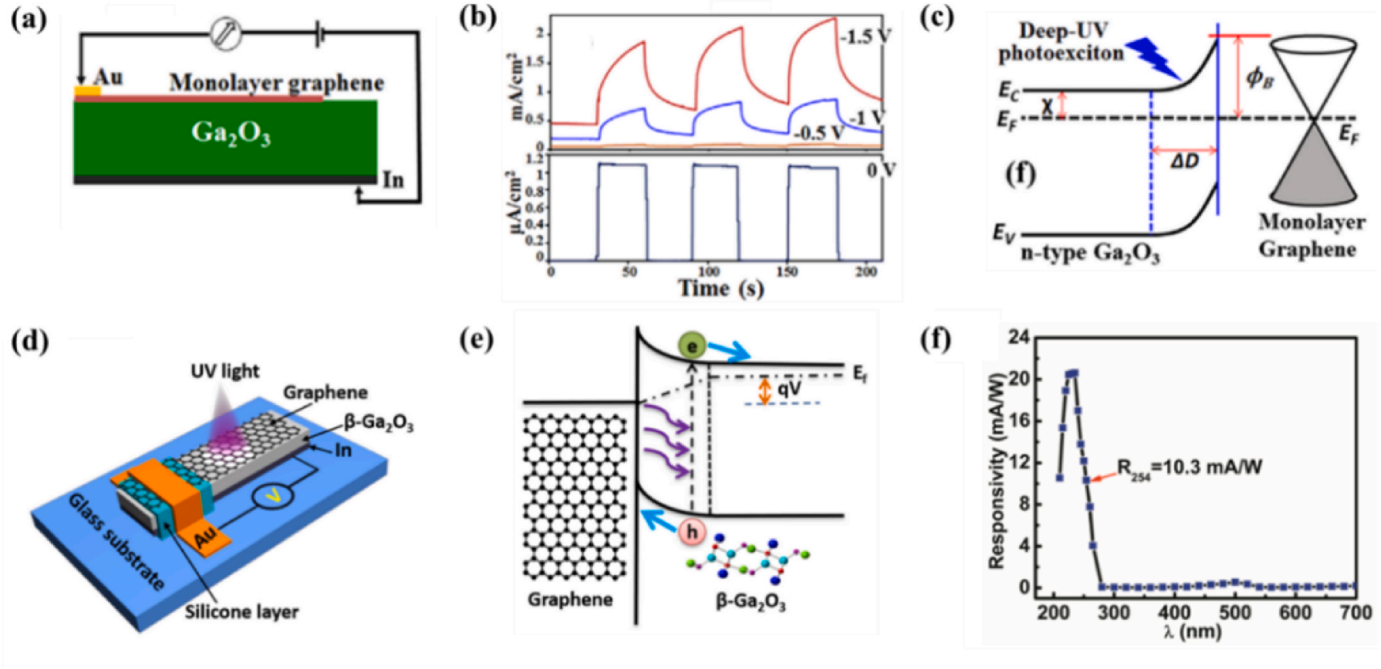

Fig. 11. (a) Schematic diagram of fabricated graphene/β-Ga_2O_3 vertical Schottky junction photodetector. (b) Transient response for the device at different voltages. (c) Corresponding energy band diagram of graphene/β-Ga_2O_3 [57]. (d) The structure diagram of graphene/β-Ga_2O_3 vertical structure photodetector. (e)The energy band diagram under the solar-blind UV illumination at zero bias. (f) Spectral response obtained at zero bias [58].

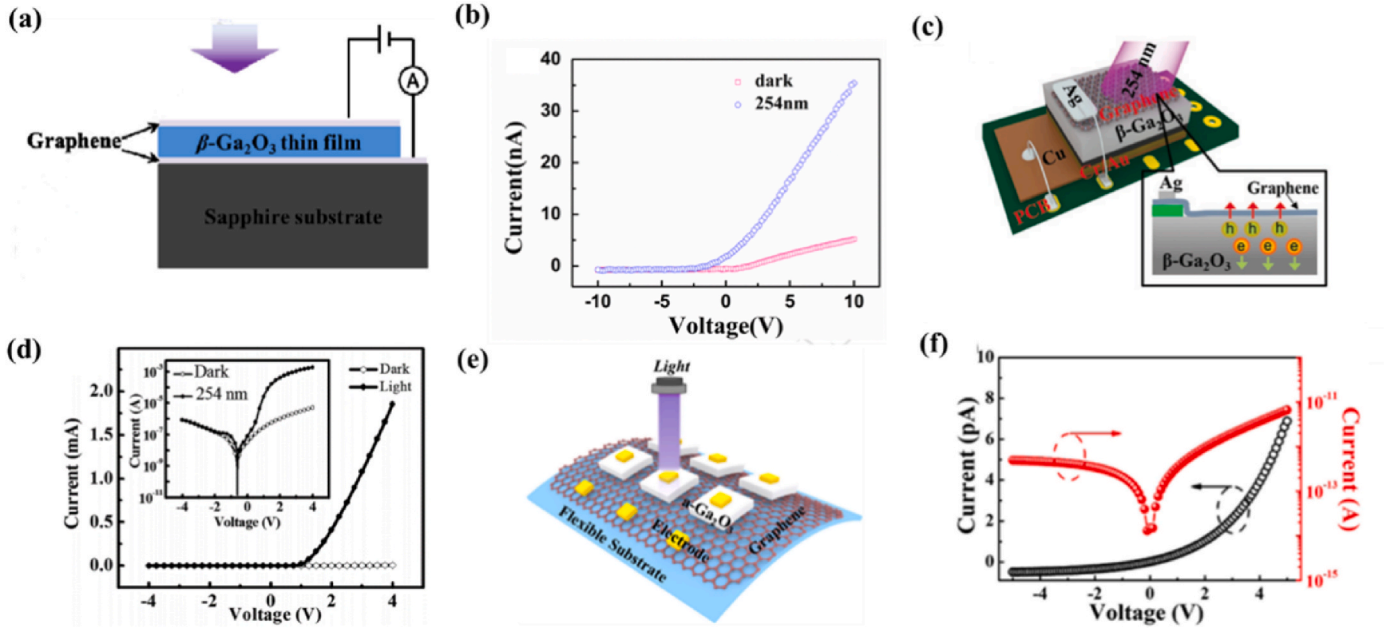

Fig. 12. (a) Cross-sectional view of the Schottky junction photodetector based on graphene/β-Ga_2O_3/graphene. (b) *I–V* characteristics curves of vertical graphene/β-Ga_2O_3/graphene device under dark and 254 nm illumination [59]. (c) Schematic diagram of the monolayer graphene/β-Ga_2O_3 photodetector. (d) *I–V* characteristics of the monolayer graphene/β-Ga_2O_3 device in dark and under 254 nm light irradiation, the inset shows the *I–V* curves on a logarithmic scale [60]. (e) Illustration of the device design and material characterizations for the graphene/a-Ga_2O_3 photodetector. (f) *I–V* curves of the graphene/a-Ga_2O_3 photodetector with both linear and logarithmic scales in the dark [61].

fabricated a graphene/β-Ga_2O_3 solar-blind photodetector by transferring a monolayer graphene on a Ga_2O_3 substrate (Fig. 12(c)) [60]. The responsivity and detectivity of the device at 20 V are 39.3 A/W and 5.92×10^{13} Jones, respectively (Fig. 12(d)). In 2020, Wang et al. fabricated a flexible photodetector based on a graphene/amorphous Ga_2O_3 structure. The photodetector exhibits a respectively of 2.75 A/W with a detectivity of 8.4×10^{13} Jones under a bias voltage of 5 V (Fig. 12 (e) and (f)) [61].

5. Heterojunction type Ga_2O_3 based self-powered photodetectors

Due to the difficulty of the p-type doping of Ga_2O_3, it is challenging to construct a pn or pin β-Ga_2O_3 homojunction for opto-/electronic

applications. Hence, choosing a p-type semiconductor or a larger band offset n-type semiconductor to build a pn or nn heterojunction is an alternative method to fabricate the Ga_2O_3 based self-powered photodetectors. The band alignment between the semiconductor and Ga_2O_3 should be considered first to construct a heterojunction type self-powered photodetector. Up to now, Ga_2O_3 heterojunction type photodetectors have been reported by combining with other inorganic semiconducting materials, including GaN, ZnO, diamond, etc., as well as organic materials, including PEDOT: PSS and Spiro-MeOTAD.

5.1. All-inorganic type heterojunction

Nb doped $SrTiO_3$ single crystals (NSTO) have a large bandgap (3.2 eV) and can form a type II heterojunction with Ga_2O_3 [62–64]. In 2016, our group built a β-Ga_2O_3/NSTO heterojunction photodetector (Fig. 13 (a) and (b)) [65]. The device exhibits the solar-blind photoelectric properties at zero bias with a maximum PDCR of 20 under solar-blind light illumination. Compared with NSTO, diamond has a larger bandgap (5.5 eV) and is a natural solar-blind material. In 2018, Chen et al. constructed the diamond/β-Ga_2O_3 heterojunction photodetector by depositing a Ga_2O_3 epitaxial film on a CVD-grown diamond substrate [66]. The device's *I–V* curves show typical rectification characteristics, suggesting that the heterojunction was effectively created. The photodetector exhibit a cutoff responsivity wavelength of 270 nm, and a UV/visible rejection ratio exceeded two orders of magnitude at 0 V (Fig. 13(c) and (d)). To develop photodetectors, 2D layered transition metal dichalcogenides (TMDs) are a good choice because of their unique atomic thickness, stacking utilizing van der Waals forces, and being devoid of surface chemical dangling bonds on the surface [67–73]. In 2018, Zhuo et al. built a β-Ga_2O_3/MoS_2 heterojunction self-powered photodetector (Fig. 13(f)) [74]. The MoS_2/β-Ga_2O_3 heterojunction photodetector had a responsivity of 2.05 mA/W and a specific detectivity of 1.21×10^{11} Jones at zero bias, with a cutoff wavelength of 260 nm and a high rejection ratio of 1.6×10^3 ((Fig. 13(e) and (f)). In 2021, Wang et al. created solar-blind photodetectors by mixing stacked GaSe flakes with Ga_2O_3 epitaxial films [75] ((Fig. 13(g)). The GaSe/Ga_2O_3 heterojunction photodetector shows a high sensitivity with a responsivity of 0.19 A/W and a quick rise/fall time of 0.32/52.6 μs at 0 V (Fig. 13(h) and (i)).

A large lattice and thermal expansion coefficient mismatch may decrease the device's performance. Due to suitable energy band offsets and small lattice mismatch (<5%) between ZnO and Ga_2O_3, ZnO/Ga_2O_3

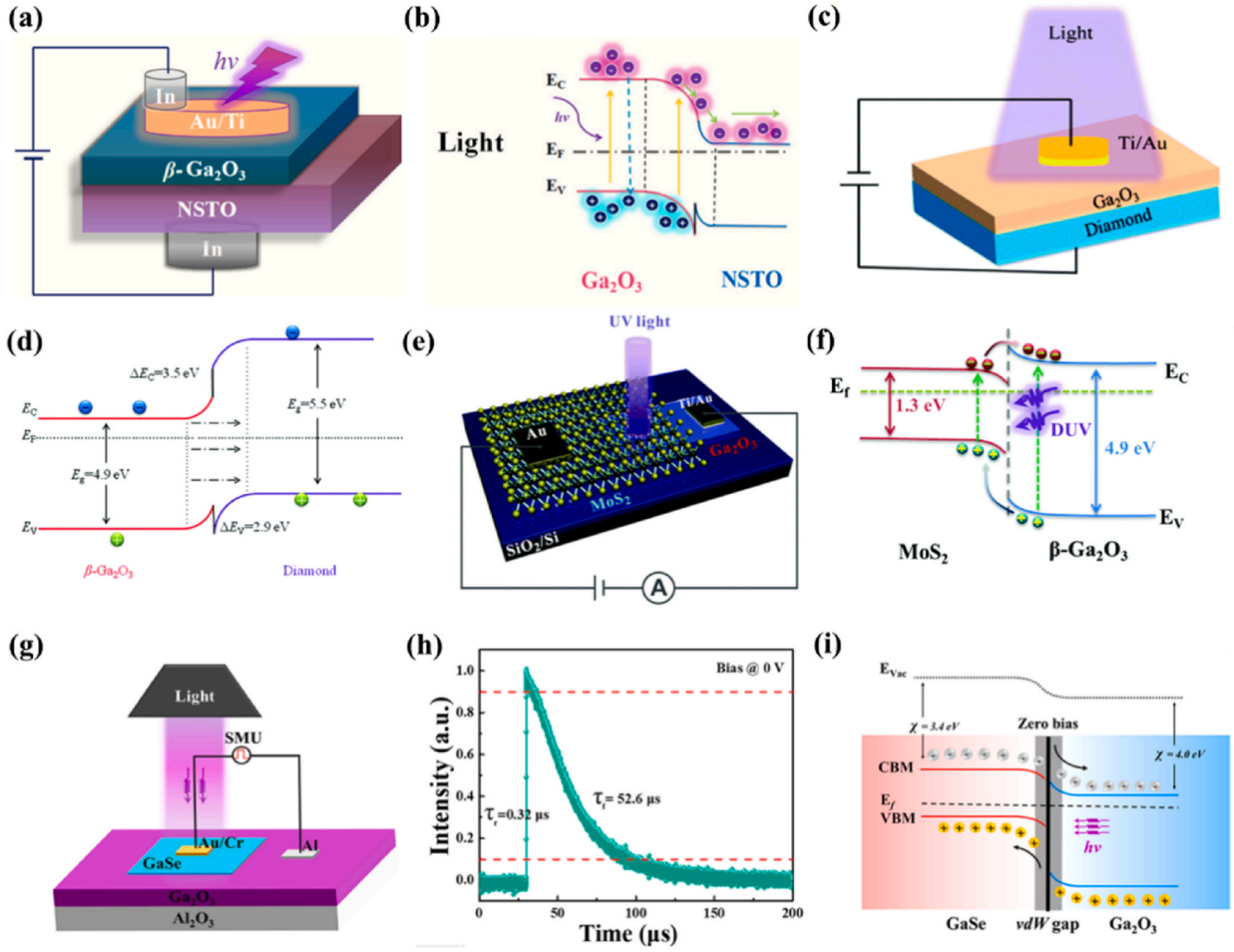

Fig. 13. (a) Schematic illustration of β-Ga_2O_3/NSTO heterojunction photodetector. (b) Schematic energy band diagrams of the β-Ga_2O_3/NSTO heterojunction [65]. (c) Schematic illustration of β-Ga_2O_3/diamond heterojunction photodetector. (d) Energy band diagrams of the diamond/β-Ga_2O_3 photodetector [66]. (e) A schematic illustration of a β-Ga_2O_3/MoS_2 heterojunction device. (f) Energy band diagrams of the β-Ga_2O_3/MoS_2 heterojunction under solar blind light illumination [74]. (g) A schematic illustration of a β-Ga_2O_3/GaSe heterojunction device. (i) Energy band diagrams of the β-Ga_2O_3/GaSe heterojunction under solar blind light illumination [75].

heterojunction photodetectors are promising designs. In 2017, Zhao et al. used simple one-step chemical vapor deposition to synthesize a highly crystallized ZnO-Ga_2O_3 heterojunction photodetector (Fig. 14(a)) [76]. Considering that the ZnO (900 °C) and Ga_2O_3 (1100 °C) have different growth threshold temperatures, the synthesis of the ZnO-Ga_2O_3 heterostructure could be performed in one continuous temperature-rise reaction (Fig. 14(b)). The device shows an ultrahigh responsivity (9.7 mA/W) with a sharp cutoff wavelength at 251 nm (Fig. 14(c)), a high solar-blind/visible rejection ratio (R_{251nm}/R_{400nm}) of 6.9 × 10^2 (Fig. 14 (d)), and a fast response speed of 100 μs/900 μs(Fig. 14(e)) at 0 V which is owing to the large ΔE_V (0.32 eV) and ΔE_c (1.85 eV) of the ZnO-Ga_2O_3 heterojunction (Fig. 14(f)).

In 2017, our group studied the photoelectric properties and physical mechanisms of ZnO-Ga_2O_3 heterojunction photodetectors by sputtering a β-Ga_2O_3 layer on a ZnO crystal substrate (Fig. 14(g)) [77]. The typical characteristic rectifying *I–V* curves confirm the photovoltaic behavior in the device (Fig. 14(h)). At zero bias, the heterojunction photodetector exhibits a PDCR of about 14.8 under 254 nm light (Fig. 14(i)). However, due to many defects and dislocations in the obtained Ga_2O_3 films, the photoelectric performance was non-ideal. To improve photodetector performances, the β-Ga_2O_3/Ga: ZnO-based photodetector was constructed (Fig. 14(j)) [78]. The device exhibits an optimized performance with a notable responsivity of 0.763 mA/W and a PDCR of 127 at 0 V (Fig. 14 (k) and (l)).

GaN, a third-generation semiconductor material, has a hexagonal wurtzite structure [79,80]. Previous studies have shown that high-quality GaN can be epitaxially grown on $(\bar{2}01)$ β-Ga_2O_3 structure due to the matched lattice [81]. The O atoms on the $(\bar{2}01)$ plane of β-Ga_2O_3 is arranged in a triangle with a distance between adjacent O atoms ranges 0.286–0.304 nm while the Ga and N atoms on the (0001) plane of GaN are also arranged in a triangle with a distance between adjacent Ga atoms about 0.319 nm. Although the mismatch between them is 4.7–10.3%, the experimental results show that the Ga atoms, which are exposed on the GaN surface, can easy to combine with O atoms to form $(\bar{2}01)$ oriented β-Ga_2O_3. In 2017, GaN/β-Ga_2O_3 heterojunction photodetectors were studied [82]. As shown in Fig. 15, the energy difference between the Fermi level and the valence band maximum (VBM) of p-GaN and n-Ga_2O_3 is about 1.58 eV and 4.05 eV, respectively. Therefore, the valence band offset, and conduction band offset of GaN/Ga_2O_3 heterojunction is calculated to be 0.78 and 0.74 eV, respectively. When p-GaN and n-Ga_2O_3 are in contact, the Fermi levels line up due to the carrier transmission. As a result, a pn junction depletion layer is formed near the GaN/Ga_2O_3 interface. The responsivity, response speed, and PDCR of the self-powered solar-blind photodetector under 254 nm light are 28.44 mA/W, 0.14/0.07 s, and 74, respectively. The larger the potential barrier (qV), the better performance of the photodetector. If Ga_2O_3 is doped with tetravalent elements, the Fermi level can approach the conduction band and the built-in potential barrier in GaN/Ga_2O_3 heterojunction increases. Therefore, the solar-blind photoelectric performance of the GaN/Sn: Ga_2O_3 detector improves substantially [83]. At 0 V, the photodetector has a responsivity of 3.05 A/W, which is the greatest value recorded to date. Because of the higher number of free carriers in the Sn-doped Ga_2O_3 than that in pure Ga_2O_3, the Fermi level of GaN/Sn: Ga_2O_3 is closer to the conduction band, and the built-in potential barrier exceeds that of the GaN/Ga_2O_3 junction (Fig. 15 (f)). The larger built-in potential barrier is more effective in separating and transferring the photogenerated carriers.

The low hole mobility of Ga_2O_3 can seriously alter the response time of the photodetectors. To improve the performance of photodetectors, scientists combined Ga_2O_3 with hole transport materials. Inorganic hole transporter materials including NiO, Cu_2O, CuO, CuI, CuSCN, $CuCrO_2$, and $CuGaO_2$ were selected to form the built heterojunction with Ga_2O_3.

Copper(I) thiocyanate (CuSCN) is a p-type material with a high hole mobility of 0.01–0.1 cm^2/V·S and widely used in optoelectric devices like light-emitting diodes, solar cells, and photodetectors [84–91]. In 2019, a n-Ga_2O_3/p-CuSCN core-shell structure photodetector was constructed via immersing a β-Ga_2O_3 single-crystal microwire into a solution of p-type CuSCN (Fig. 16 (a)) [92]. At 0 V, the photodetector exhibit a responsivity and detectivity of 98 μA/W and 9.7 × 10^{10} Jones, respectively (Fig. 16 (b)). Meanwhile, the n-Ga_2O_3/p-CuSCN heterojunction shows a response speed of 0.19/0.16 s. CuI is another low-cost and stable copper-based p-type semiconductor, which can be used as hole conductor material. Similar to CuSCN, CuI has high p-type conductivity (238 S/cm), and it is solution-processable with a high hole mobility (43.9 cm^2/(V·s)) [93,94]. In 2019, Ayhan fabricated a *c*-CuI/β-Ga_2O_3 heterostructure-based photodetector. The photodetector exhibit a high open circuit voltage of 0.706 V and a photocurrent of 2.49 mA/W under a 254 nm light at zero bias [95] (Fig. 16 (d)–(f)). In 2020, a β-Ga_2O_3/CuI core-shell heterostructure photodetector was constructed using a facile immersion method. The exfoliated β-Ga_2O_3 microwire was used as both photon absorber and reactor, while the solution-processed CuI film was selected to form the built-in field and serve as hole-transport layer [96]. Its responsivity, detectivity, PDCR, and rise/decay times are 8.46 mA/W, 7.75 × 10^{11} Jones, 4.0 × 10^3 and 97.8/28.9 ms, respectively, under 254 nm light at zero bias (Fig. 15 (g) and (h)). The first-principle calculations were used to better understand the underlying self-powered and carrier transfer physical mechanisms. In the 3D differential charge density of the Ga_2O_3 (100)/CuI (111) interface (Fig. 16 (i)), the charge-producing (yellow) and charge-depleting regions (cyan) are near the interface even without the applied bias, which indicates that the charge redistribution of the diffusion occurs at the interface and causes the formation of an electric dipole. The existence of a charge depletion region near the interfacial Ga atoms and a charge obtained region surrounding the interfacial Cu atoms indicates that the Ga_2O_3 is positively charged while CuI is negatively charged. The delafossite semiconductor materials $CuGaO_2$ and $CuCrO_2$ have become well-known because of their wide bandgap and fast hole diffusion coefficient, widely used in solar cells and catalysts [97–107]. $CuGaO_2$ and $CuCrO_2$ can form a type II staggered band alignment with n-type β-Ga_2O_3. In addition, the fast hole diffusion coefficients of $CuGaO_2$ and $CuCrO_2$ can guarantee the transport of holes. However, highly crystalline $CuMO_2$ is challenging to obtain via conventional synthesis methods, including solid-state reactions and vacuum-deposition techniques. In 2020, we prepared solar-blind photodetectors based on $CuMO_2$/β-Ga_2O_3 (M = Ga^{3+}, Cr^{3+}) heterojunction [108]. At zero bias, the $CuGaO_2$/β-Ga_2O_3 and $CuCrO_2$/β-Ga_2O_3 pn photodetectors show photoresponse time of 0.14 s/0.06 s, a high PDCR of 2.3 × 10^4/3.5 × 10^4 and a high rejection ratio ($R_{254\ nm}/R_{365\ nm}$) of 2.0 × 10^4/2.8 × 10^4 (Fig. 16 (j)–(l)).

NiO is another p-type hole-transport material with superior thermal and chemical stability [105–113]. Due to the low-cost, easy synthesis, NiO thin films have been widely studied, and several NiO/Ga_2O_3 heterojunction photodetectors were reported. In 2020, a radio-frequency (RF) reactive magnetron sputtering system was used to fabricate an all-oxide NiO/Ga_2O_3 heterojunction at room temperature [114]. Thanks to the novel design, the photodetector exhibits a photoresponse time of 0.34 s and a PDCR of 122 under 254 nm light at zero bias (Fig. 17 (a) and (b)). The valence band offset and conduction band offset at the NiO/-Ga_2O_3 heterojunction were calculated to be 3.02 and 1.82 eV, respectively, which indicates that a type II heterojunction was formed (Fig. 17 (c)). The photodetector shows a faster response speed and lowers photocurrent under vacuum conditions than in a pure oxygen environment. These observations can be explained by surface defects such as oxygen vacancies that can act as trapping sites. In the dark, O_2 molecules, which were absorbed in these sites, form O^{2-}[O_2 + e^-→O^{2-}]. Furthermore, when the films are exposed to light, the photogenerated holes migrate to the surface and recombine with negatively charged O_2 molecules, leaving unpaired electrons in the films that contribute to the photocurrent. Yu et al. used the surface plasmon effect of Pt nanoparticles to improve the Ga_2O_3/NiO heterojunction's photoresponse performance (Fig. 17 (d)) [115]. The use of surface plasmons is an

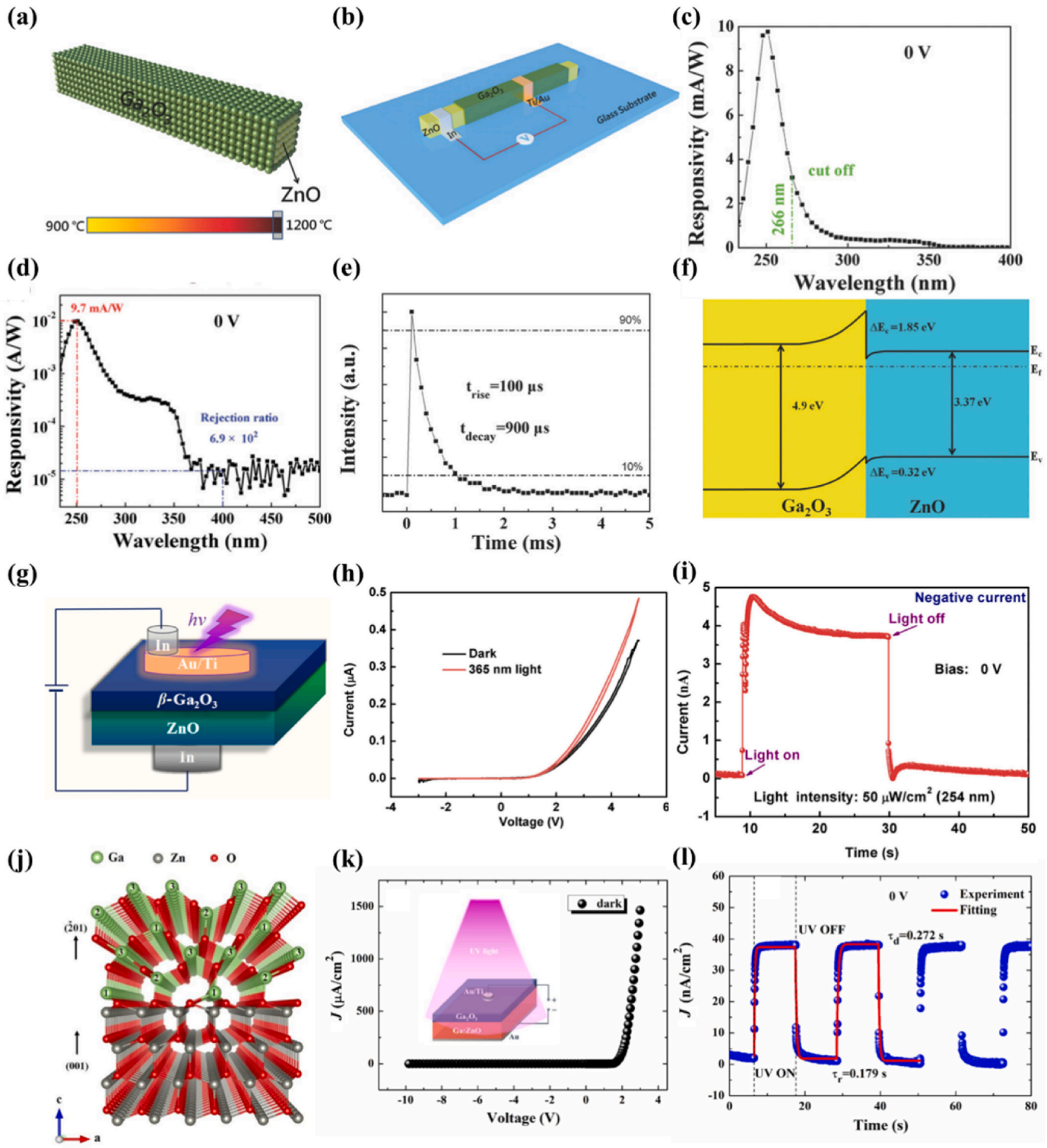

Fig. 14. (a) The schematic diagram of the growth process of ZnO-Ga_2O_3 core-shell microwire. (b) The schematic diagram of the ZnO-Ga_2O_3 core-shell heterojunction photodetector device. (c) The photoresponse spectrum of the device at 0 V and (d) its spectrum in a log coordinate. (e) The time response under the excitation of 266 nm pulse laser at 0 V. (f) The energy band diagram of the ZnO-Ga_2O_3 core-shell heterojunction device [76]. (g) Schematic illustration of β-Ga_2O_3/ZnO heterojunction photodetector. (h) *I–V* characteristic curves of the β-Ga_2O_3/ZnO heterojunction photodetector in dark and under 365 nm light. (i) Time-dependent photoresponse of the β-Ga_2O_3/ZnO heterojunction photodetector [77]. (j) Schematic representation of atoms arrangement on the β-Ga_2O_3/Ga:ZnO heterojunction. (k) The C–V characteristics of the β-Ga_2O_3/Ga:ZnO heterojunction under dark. (l) Time-dependent photoresponse and the corresponding exponential fitting of the heterojunction under 254 nm illumination at zero-bias [78].

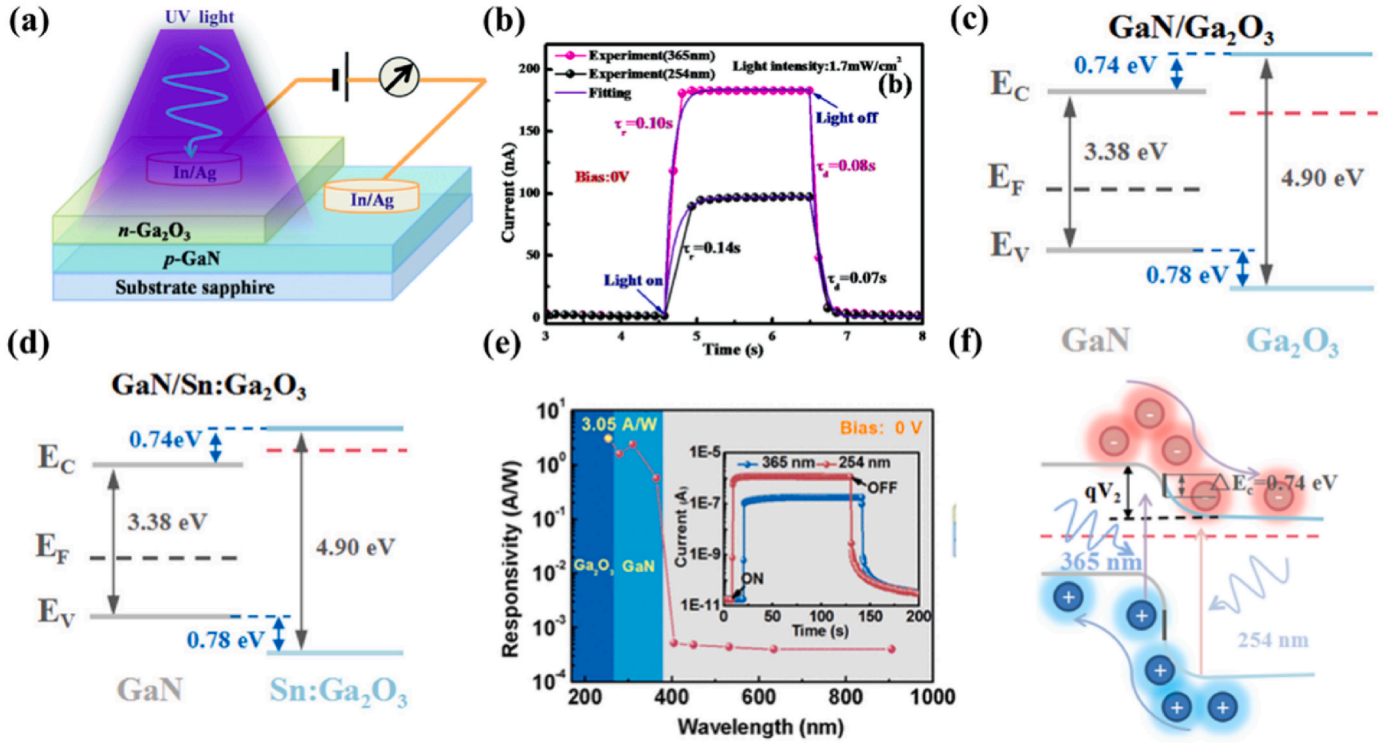

Fig. 15. (a) The schematic illustration of the fabricated prototype β-Ga_2O_3/GaN p-n junction photodetector. (b) The time-dependent photoresponse of the photodetector at zero bias and the corresponding exponential fitting. (c) Schematic energy band diagrams of the β-Ga_2O_3/GaN p-n junction [82]. (d) The schematic illustration of the fabricated GaN/Sn:Ga_2O_3 p-n junction photodetector. (e) Wavelength selectivity of the photodetector under zero bias. (f) Schematic energy band diagrams of the GaN/Sn:Ga_2O_3 p-n junction [83].

essential technique for improving the performance of photodetectors because of the interaction that takes place between surface plasmons and light at the interface between metal and dielectric [116–119]. The Pt NPs modified photodetector exhibits enhanced performances with a high PDCR of 1492, a high responsivity of 4.24 mA/W, and a fast response speed of τ_r/τ_d about 4.6 ms/7.6 ms at 0 V (Fig. 17 (e)). Pt NPs enhanced the Ga_2O_3/NiO photodetector photoresponse for the following reasons 1) Without light, Pt NPs can form a Schottky barrier with Ga_2O_3 to inhibit the electron transport, which reduces the dark current. 2) For solar-blind light illumination, Pt NPs can trap a large amount of light and excite localized surface plasmon resonance (LSPR) and strong local electromagnetic fields. The recombination rate of photogenerated carriers may be decreased by the combined impact of LSPR and local electromagnetic fields, which can also improve the interaction of incoming light with Pt NPs. 3) Pt NPs accelerate the generation rate and separation speed of charges by increasing the absorption cross-section of the Ga_2O_3 layer.

Because the behavior of the carrier is essential to the process of photoelectric conversion, charge-carrier engineering might be a feasible technique for developing high-performance photodetectors. In 2022, the VO_x/Ga_2O_3 heterojunction-based photodetector was built using a solution-processed method [120]. It was shown that the VO_x films showed variable conductivities at various annealing conditions, which were due to changes in the regulation of crystallinities and phase structures. These changes, in turn, affected the VO_x/Ga_2O_3 photodetectors, causing variable photodetection characteristics. The modulated photodetector achieved an improved PDCR of 1.08×10^8, an $R_{245\ nm}/R_{400\ nm}$ rejection ratio of 3.12×10^4, and a responsivity of 28.9 mA/W (Fig. 18(a)-(c)). In addition, $Ga_2O_3/SrSnO_3$ heterojunction-based photodetector was also constructed [121]. $SrSnO_3$ was annealed in an oxygen atmosphere and doped with Y elements to remove oxygen vacancies and increase conductivity to increase carrier transportation effectiveness. After treatment, the oxygen vacancy in $SrSnO_3$ annealed under oxygen fell from 54.2% to 22.8%, while the conductivity in Y–$SrSnO_3$ improved by roughly one order of magnitude. The photodetector exhibits excellent photoelectrical performances with a PDCR of 4.3×10^6 and a detectivity of 1.3×10^{13} Jones (Fig. 18 (d)–(f)).

5.2. Organo-inorganic hybrid type heterojunction

The preparation process of conventional all-inorganic photodetectors is complicated and requires high temperatures, high vacuum, and complex lithography, leading to expensive device manufacturing costs. Moreover, inorganic materials' fragile and hard properties limit their application where large areas and flexibility are needed. Coincidentally, the organic-inorganic heterojunction has become one of the most promising designs after many years of progress. Organic self-powered photodetectors made of solution-processable materials may be made inexpensively and allow for large-area deposition. Organic-inorganic hybrid heterojunctions maintain the benefits of the high conductivity of the inorganic components and use the advantages of organic features such as flexibility and biocompatibility. Thanks to the improved design, various organic materials such as Spiro-MeOTAD, PANI, PEDOT: PSS, and so on were used to fabricate organic-inorganic hybrid heterojunctions with a wide selection of inorganic semiconductors [122–131].

Polyaniline (PANI) is an excellent p-type conducting polymer with large hole mobility under different doping concentrations. Wang et al. realized a self-powered solar-blind UV photodetector by a facile combination of a centimeter-sized single crystal β-Ga_2O_3 microwire and polyaniline in 2020. Owing to the excellent organic/inorganic hybrid p-n junction, the device shows an responsivity of 21 mA/W at 246 nm with a sharp cut-off wavelength of 272 nm without an external power supply. Moreover, the dark current is 0.08 pA and the UV/visible rejection ratio reaches 10^2 at zero bias voltage [132].

PEDOT: PSS with high conductivity of 830 S/cm and hole mobility of 1.7 $cm^2/V{\cdot}S$ is a superb p-type conductive polymer [133,134]. In

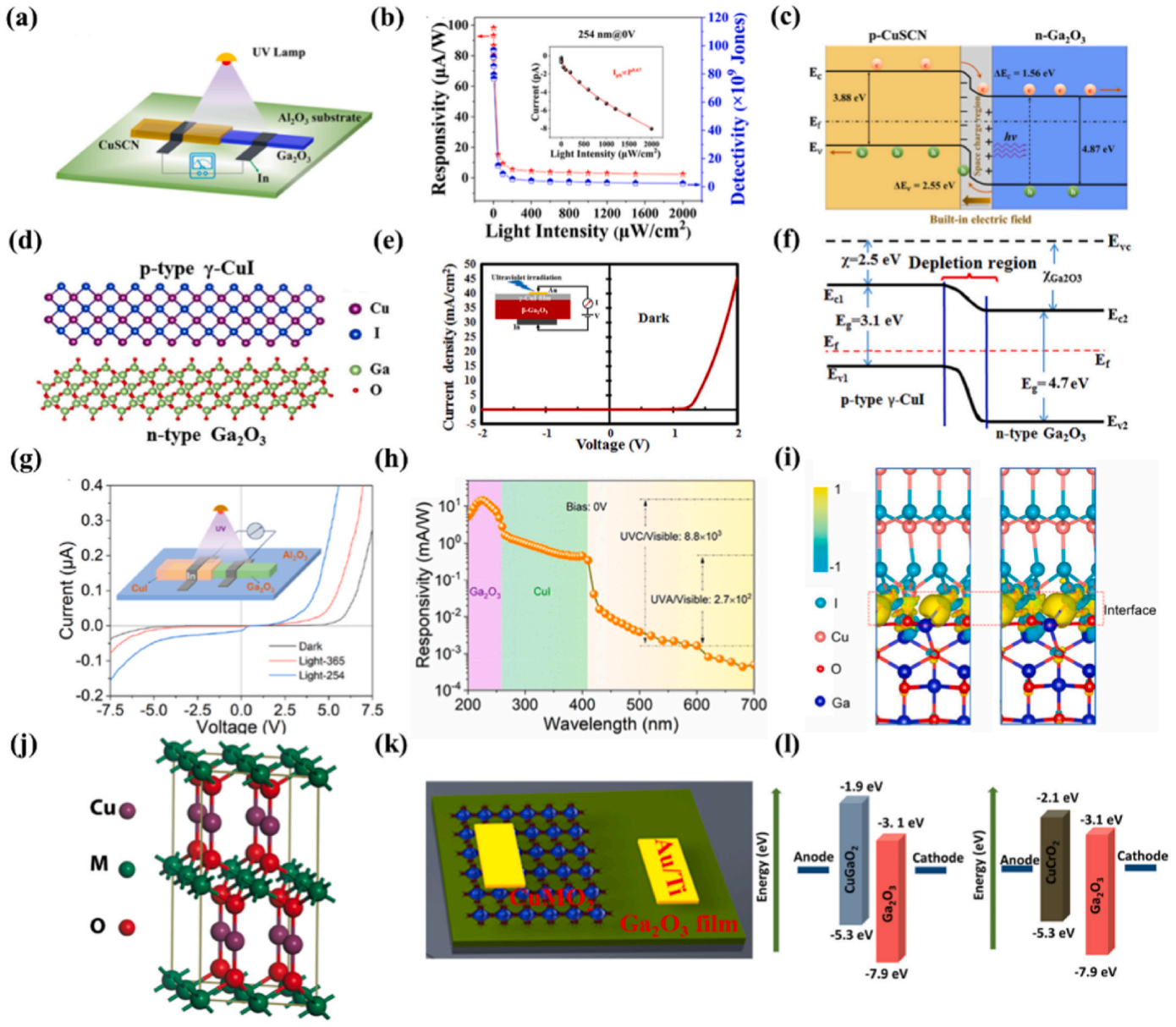

Fig. 16. (a) Schematic diagram of the Ga_2O_3/CuSCN core-shell microwire heterojunction photodetector. (b) Responsivity and detectivity as a function of the light intensities under bias voltages 0 V. (c) Schematic photoelectric mechanism of the Ga_2O_3/CuSCN heterojunction under solar-blind waveband illumination [92]. (d) Ball and stick diagram of γ-CuI and β-Ga_2O_3 heterostructure. (e) C–V characteristic curves of the γ-CuI/β-Ga_2O_3 heterojunction photodetector in dark. (f) Schematic diagram and corresponding energy band diagram of γ-CuI/β-Ga_2O_3 heterostructure photodetector [95]. (g) Schematic diagram of the CuI/β-Ga_2O_3 core–shell photodetector. (h) Wavelength selectivity of the photodetector under zero bias. (i) Charge density difference of the Ga_2O_3 (100)/CuI (111) interface without and with electric field [96]. (j) Crystal structure of $CuMO_2$. (k) The schematic illustration of the $CuMO_2$/β-Ga_2O_3 pn junction. (l) Energy band diagrams of the $CuGaO_2$/β-Ga_2O_3 and $CuCrO_2$/β-Ga_2O_3 pn junction [108].

addition, their simple fabrication process and commercial availability made them the preferred organic material for photodetectors. Zhang and co-workers spin-coated an organic conductive PEDOT: PSS on the Ga_2O_3 film to fabricate a high-performance PEDOT:PSS/Ga_2O_3/p-Si heterojunction photodetector for the first time in 2019 (Fig. 19 (a)) [135]. At 0 V bias, the PEDOT: PSS/Ga_2O_3/p-Si hybrid solar-blind photodetector shows an external quantum efficiency (EQE), which was higher than that of the Ga_2O_3 photovoltaic devices reported previously. The device shows a sensitive solar-blind spectral selectivity with a solar-blind/visible rejection ratio ($R_{255\ nm}/R_{405\ nm}$) of 450 (Fig. 19 (b)). Unlike the previously reported heterojunction photodetectors, this device had two built-in electrical fields (PEDOT:PSS/Ga_2O_3 and Ga_2O_3/Si junction), which can effectively enhance the separation efficiency of photogenerated carriers in the space charge region of Ga_2O_3(Fig. 19 (c)).

Inspired by the above work, researchers attempted to fabricate a Ga_2O_3-based organic-inorganic heterojunction photodetector. Ga_2O_3 thin film deposited on a Si substrate shows a disordered growth orientation and poor crystallization. This cause the hybrid photodetector to suffer from a large dark current and noise, which could negatively affect the photodetector's detectivity. To overcome this problem, new PEDOT: PSS/Ga_2O_3 hybrid heterojunction photodetectors were reported by Wang and our group, respectively. In 2019, Wang et al. built a PEDOT: PSS/Ga_2O_3 microwires photodetector (Fig. 19 (c)) [136]. The Ga_2O_3 microwires were synthesized using a CVD with a length of 6–9 mm and an average diameter of about 10 μm. Without a power source, the device exhibits ultrahigh responsivity of 2.6 A/W at 245 nm with a sharp cutoff wavelength at 255 nm (Fig. 19 (d)). The device exhibits an ultrahigh solar-blind/UV rejection ratio ($R_{245\ nm}/R_{280\ nm}$) of 10^3. The depletion

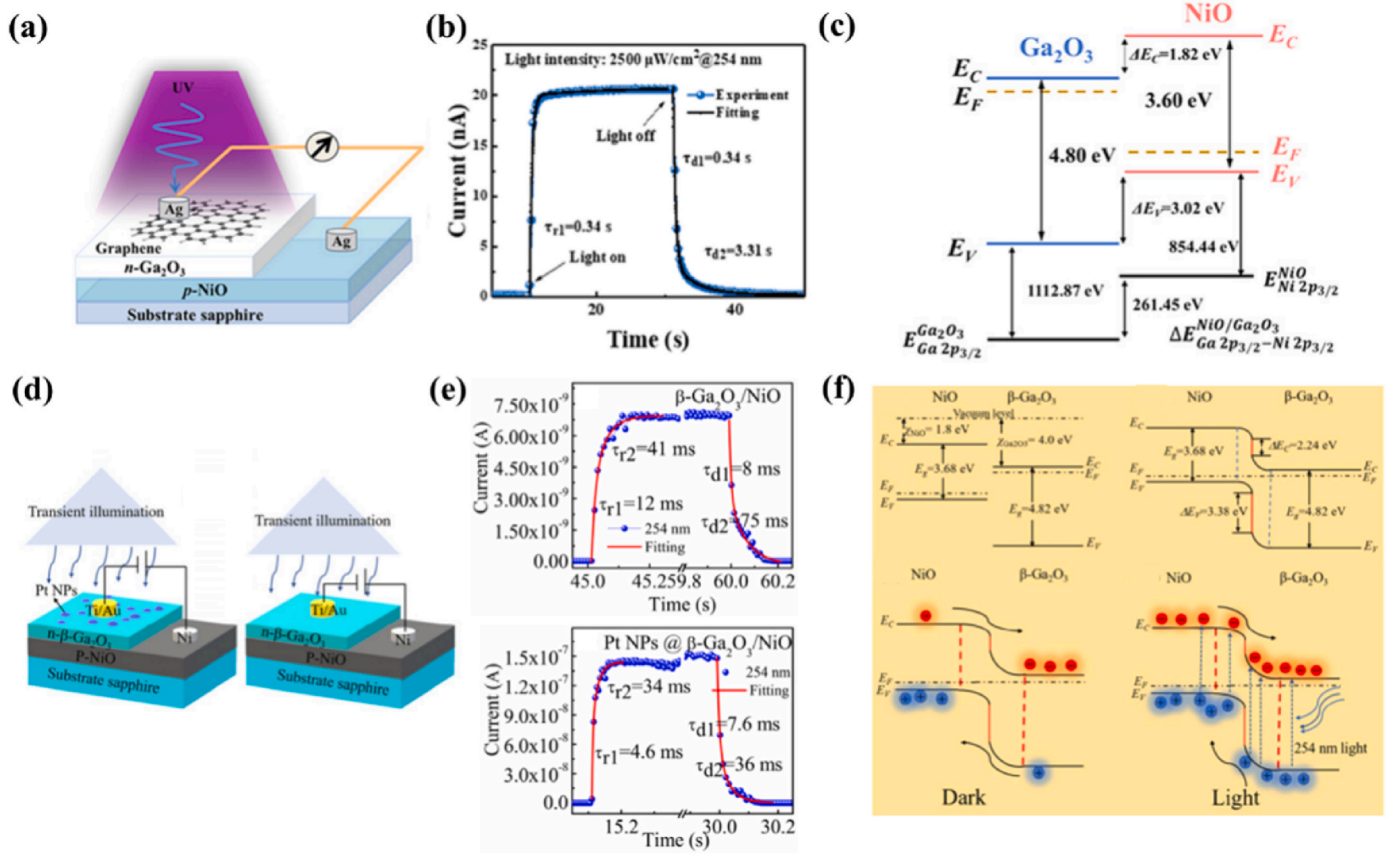

Fig. 17. (a) Schematic illustration of the fabricated NiO/Ga_2O_3 p-n junction. (b) Enlarged view of the rise/decay edges and the corresponding exponential fitting. (c) Schematic representation of the band alignment at the NiO/Ga_2O_3 p-n junction interface [114]. (d) Schematic of the β-Ga_2O_3/NiO heterojunction with and without Pt NPs. (e) The exponential curves fitting of the rise and decay time of β-Ga_2O_3/NiO heterojunction photodetector without and with metal Pt NPs. (f) Energy band diagrams for isolated NiO and β-Ga_2O_3 [115].

layer of the heterojunction is mainly on the Ga_2O_3 side, and the PEDOT: PSS has no optical response at any wavelength in this study, so the PEDOT: PSS/Ga_2O_3 photodetector has the same cutoff edge as the pure Ga_2O_3 device and has a high rejection rate. In 2019, our group constructed a PEDOT:PSS/Ga_2O_3 heterojunction photodetector via a cost-effective solution method (Fig. 19 (g)) [137]. The Ga_2O_3 films were fabricated using a modified MOCVD system and treated using air plasma to obtain a clean and hydrophilic surface. Therefore, uniform thick PEDOT: PSS can be obtained using spin coating PEDOT: PSS solution on Ga_2O_3. Such a clean and uniform interface facilitates efficient charge carrier transport. Furthermore, by employing the oxygen implantation effect, the air plasma may eliminate the oxygen vacancy defects at the surface of the Ga_2O_3 film, improving photodetector performance. The organic-inorganic hybrid photodetector shows excellent self-powered detection performance in the solar-blind region with a large R_{250nm}/R_{360nm} rejection ratio of 7×10^3, and a detectivity of 9.2×10^{12} Jones at 0 V (Fig. 19 (h)). In addition, due to the positive effect of the strong photovoltaic effect, the hybrid photodetector displays a high EQE of 18.3%, excellent responsivity of 37.4 mA/W, and a superfast response speed with rise time of 3.3 μs. The device's V_{oc} is practically constant at 0.9 V, which is consistent with the idea that the maximum V_{oc} of photovoltaic devices is only dependent on interfacial energy-level alignment. The V_{oc} of the PEDOT: PSS/Ga_2O_3 hybrid heterojunction is much larger than that of previous Ga_2O_3-based heterojunctions (Fig. 19 (i)).

Spiro-MeOTAD is another attractive hole-conductor polymer with high-conductivity, nontoxic, and solution-processable and is widely used in optoelectric devices like solar cells or LEDs [138–144]. In 2020, Spiro-OMeTAD/Ga_2O_3 based self-powered solar-blind photodetector was formed (Fig. 20 (a)) [145]. The CB and the VB of Ga_2O_3 are higher than the lower unoccupied molecular orbital (LUMO) and highest occupied molecular orbital (HOMO) of Spiro-MeOTAD, respectively. This band alignment is a benefit for carrier separation and transport. Under solar-blind light illumination, photoinduced electron and hole pairs were rapidly separated by the built-in electric field, and the electrons transferred from the VB of Ga_2O_3 to the HOMO of Spiro-MeOTAD while the holes transferred from LUMO of Spiro-MeOTAD to the CB of Ga_2O_3 subsequently (Fig. 20 (b)). The device exhibits a high responsivity of 65 mA/W, an EQE of 32%, and a fast response speed of 2.98/28.49 μs at 0 V (Fig. 20(c) and (d)). Small-molecule hole transport materials (SMHTMs) were also used to prepare organo-inorganic hybrid type heterojunction photodetectors with Ga_2O_3. In the construction of photodetectors with Ga_2O_3, four different types of SMHTMs have been used, and all of them exhibit self-powered characteristics with a PDCR of about 10^5 [146]. Among them, the photodetector based on β-Ga_2O_3/-TAPC heterojunction shows the best photoelectrical performances with a dark current of about 20 fA, an I_{on}/I_{off} ratio of 5.9×10^5, and a detectivity of 1.02×10^{13} Jones at 0 V.

5.2.1. *Phase junction type self-powered Ga_2O_3 based photodetectors*

Given the several polymorphic forms of Ga_2O_3, it is possible to create Ga_2O_3 photodetectors based on different phases. The low lattice mismatch between the two phases of Ga_2O_3 can ease the issue of poor epitaxial film quality. In addition, the bandgap of the two phases is comparable, which means that the spectral response of the created junction will match the solar-blind region with a higher degree of accuracy.

The α/β-Ga_2O_3 phase junction has been investigated for application

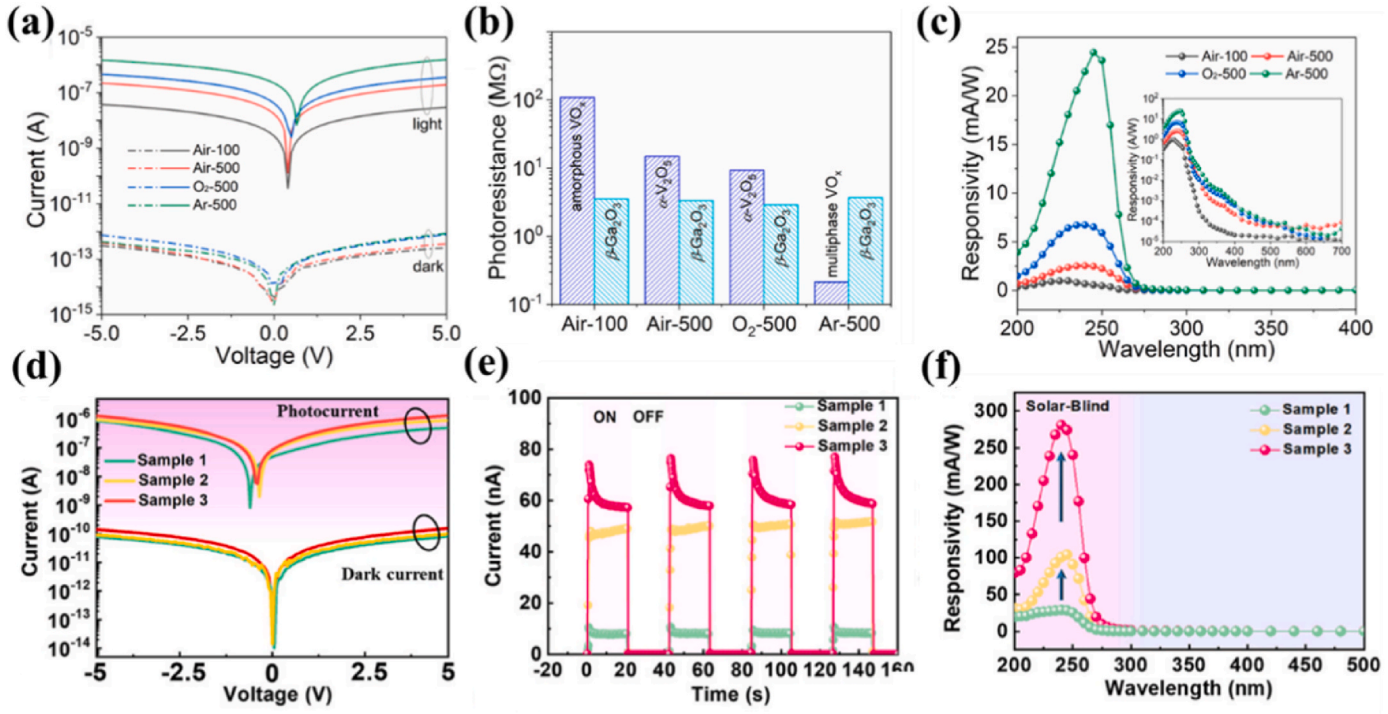

Fig. 18. (a) *I–V* curves of VO_x/Ga_2O_3 photodetectors under dark and light. (b) Resistances of VO_x and Ga_2O_3 under light. (c) Self-powered spectral responsivities of VO_x/Ga_2O_3 photodetectors [116]. (d) *I–V* curves of $SrSnO_3/Ga_2O_3$ photodetectors under dark and light. (e) *I-t* curves of $SrSnO_3/Ga_2O_3$ photodetectors under 0 V. (g) Spectral responsivities of $SrSnO_3/Ga_2O_3$ photodetectors [117].

in solar-blind photodetectors. A low-cost hydrothermal and post-annealing treatment technique is used to build the α/β phase junction of Ga_2O_3 vertically aligned nanorod arrays (NRAs) with a thickness-controllable β-Ga_2O_3 shell layer [147]. As shown in Fig. 21 (a), the precursor GaOOH NRAs were generated using a simple hydrothermal approach using FTO as the substrate, then annealed and dehydrated at 450 °C to yield porous sub-stable α-Ga_2O_3 NRAs ($2GaOOH \Rightarrow Ga_2O_3+H_2O$). The seed layer thickness, solution concentration, and development period may influence the density, diameter, and length of α-Ga_2O_3 NRAs. When the porous α-Ga_2O_3 NRAs are placed in the700 °C furnace, the α-phase Ga_2O_3 on the surface layer is instantly changed into β-phase Ga_2O_3. Because Ga_2O_3 has a low thermal conductivity, the temperature of the inner layer of the NRAs rises slowly, allowing the α-phase to persist (Fig. 21 (b) and (c)). Utilizing the α/β-Ga_2O_3 NRAs, our group developed solar-blind photodetectors with graphene-silver nanowire hybrid conductive electrodes, as illustrated in Fig. 21 (d) [148]. Thanks to the small lattice mismatch (<3%) as well as the high conductivity and optical transmittance of the top electrode, the photodetectors show a high PDCR of about 2000 and a high rejection ratio ($R_{254\ nm}/R_{365\ nm}$) of 2.7×10^3 at 0 V (Fig. 21 (e) and (f)).

Mitra report on the synthesis of novel core-shell amorphous gallium oxide nanoparticles (NPs) (a-Ga_2O_x/GaO_x NPs) that have not been previously obtained. The amorphous gallium oxide NPs were synthesized from gallium nitride using the femtosecond laser ablation in liquid technique. Transmission electron microscopy and electron energy-loss spectroscopy measurements revealed the amorphous NP nature with a Ga-rich core and oxide-rich shell. The amorphous gallium oxide NPs were used as an active layer in a solar-blind DUV photodetector with a responsivity of 15.3 mA/W in the self-powered mode.

5.2.2. Photoelectrochemical type self-powered Ga_2O_3 based photodetectors

To avoid blocking solar-blind light by the electrode, Zhang et al. designed a novel PEC self-powered photodetector using a new counter electrode as the light-receiving surface for hydrothermally synthesized α-Ga_2O_3 NRAs to enable the detection of solar-blind UV light [149]. As shown in Fig. 22 (a), quartz glass with strong deep ultraviolet light transmittance is utilized to receive optical signals and enable wavelengths below 300 nm to pass through, while Pt serves as the counter electrode by covering half of the quartz glass. The enhanced device responds from 246 to 300 nm at zero bias, with a maximum response of 0.212 mA/W at 260 nm and an $R_{260\ nm}/R_{400\ nm}$ rejection ratio of about 34. When ultraviolet light passes through the quartz and reaches the Ga_2O_3 nanorods, electron-hole pairs will be created because the nanorods will absorb photons with an energy that is greater than the gap in their bandgap. The photogenerated electron-hole pairs are separated using the built-in electric field at the interface between the α-Ga_2O_3 electrode and the electrolyte as the driving force. After that, the photogenerated holes in the α-Ga_2O_3 material flow into the electrolyte, and the negative charges that were separated are collected by the FTO along the nanorods, then introduced into the external circuit. On the other hand, the positive holes carried to the surface are captured by the hydroxide ions and go through redox processes that form redox molecules ($h^+ + OH^- \rightarrow OH^\bullet$). After that, the redox molecules travel to the surface of the Pt electrode, where they are reduced to hydroxide ions with the assistance of electrons that have been brought back into the system from the external circuit ($e^+ + OH^\bullet \rightarrow OH^-$). When compared to the hydrothermal approach, the water bath method does not need circumstances of high temperature and high pressure. It also has the benefits of having a lower cost, a more straightforward procedure, and a quicker development rate, among other benefits. A unique photoelectrochemical-type self-powered solar-blind ultraviolet photodetector was built in 2021 by Huang et al. [150] (Fig. 22 (c)). Using the water bath process, they directly produced α-Ga_2O_3 nanorod arrays without a seed layer. The device displayed a high PDCR, responsivity, and detectivity, with respective values of 1.01×10^3, 11.34 mA/W, and 2.68×10^{11} Jones. The β-Ga_2O_3 NRAs PEC self-powered solar-blind photodetector demonstrates superior photoelectric performance with a responsivity of 3.81 mA/W, a PDCR ratio of 28.97, and a photoresponse decay time less than 0.2 s (Fig. 22 (d)–(f)) [151].

PEC devices have an issue with interfacial charge recombination,

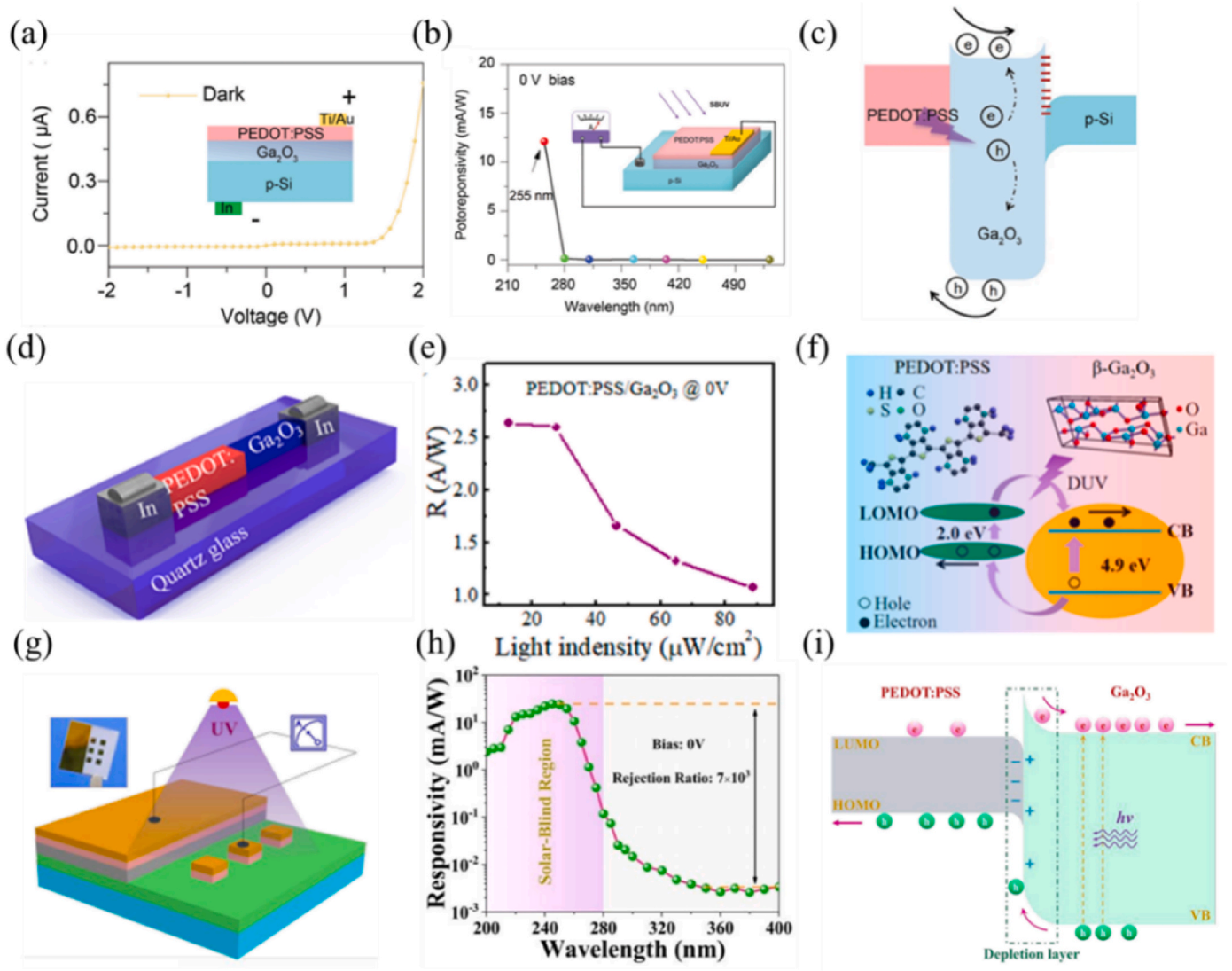

Fig. 19. (a) *I–V* characteristics of the PEDOT:PSS/Ga_2O_3/Si in dark state. (b) Spectral response of the device at 0 V bias. (c) Energy band diagram of the device at 0 V and under solar-blind solar blind illumination [135]. (d) Schematic diagram of the PEDOT:PSS/Ga_2O_3 core-shell heterojunction photodetector. (e) Responsivity of pn junction device under different light intensity. (f) Band alignment of the PEDOT:PSS/Ga_2O_3 type-II heterojunction [136]. (g) Schematic diagram of the PEDOT:PSS/Ga_2O_3 hybrid photodetector, the inset is the picture of a real prototype device. (h) Spectral response of the hybrid photodetector at 0 V. (i) Schematic energy band diagrams of the PEDOT:PSS/Ga_2O_3 hybrid heterojunction [137].

which results in a loss of photogenerated electrons. Because of their rapid carrier separation and injection into the photoanodes, semiconductor core-shell structures with type-II band alignment have recently garnered a lot of attention as the fundamental building blocks for the fabrication of next-generation electronics. Zhang et al. reported a novel tree-like branched structure made of α-Ga_2O_3 covered by γ-Al_2O_3, which had been successfully fabricated by a simple two-step hydrothermal treatment and applied to the self-powered PEC solar-blind photodetector [152] (Fig. 23 (a)). This structure was created successfully by using hydrothermal treatment. An energy barrier has been established at the semiconductor/electrolyte interface due to introducing a layer of α-Al_2O_3 with an ultra-wide bandgap to coat the outside of a layer of α-Ga_2O_3(Fig. 23 (b)). This barrier has accelerated the separation of photogenerated carriers and suppresses interfacial charge recombination. In addition, the tree-like branched structure obtained significantly increases the contact surface area between the carriers and the electrolyte. This helps shorten the charge transport distance, improving response speed and bringing a larger specific surface area, which increases light absorption. Under 254 nm, the α-Ga_2O_3/γ-Al_2O_3 heterojunction PEC photodetector shows an *R* of 0.17 mA/W, a PDCR ratio of 51.3, and a photoresponse decay time less than 0.1 s.

In our previous work, we found that a self-powered spectrum-distinguishable PEC type photodetector may be created using an α-Ga_2O_3 nanorod array (NA)/Cu_2O microsphere (MS) p-n junction [153] (Fig. 23 (d)). At 0 V, the photodetector exhibits an opposing direction of photocurrent in response to 254 and 365 nm UV light irradiation due to the combined effect of the built-in electric field of the p-n junction and the semiconductor/electrolyte junction. The photodetector responds with a responsivity of 0.42 mA/W when exposed to UV light with a wavelength of 254 nm and 0.57 mA/W when exposed to 365 nm (Fig. 23 (d) and (e)).

5.2.3. *Summary and perspective*

Solar-blind detection has attracted considerable attention, owing to its versatile applications in civilian infrastructures, military facilities, and scientific research [154-160]. Ga_2O_3, with the characteristic of ultrawide-bandgap, stable and low-cost, is an ideal candidate for solar-blind photodetector. Constructing self-powered devices that can independently, wirelessly, and energy-savingly is a significant research direction for the next-generation photodetectors and has attracted

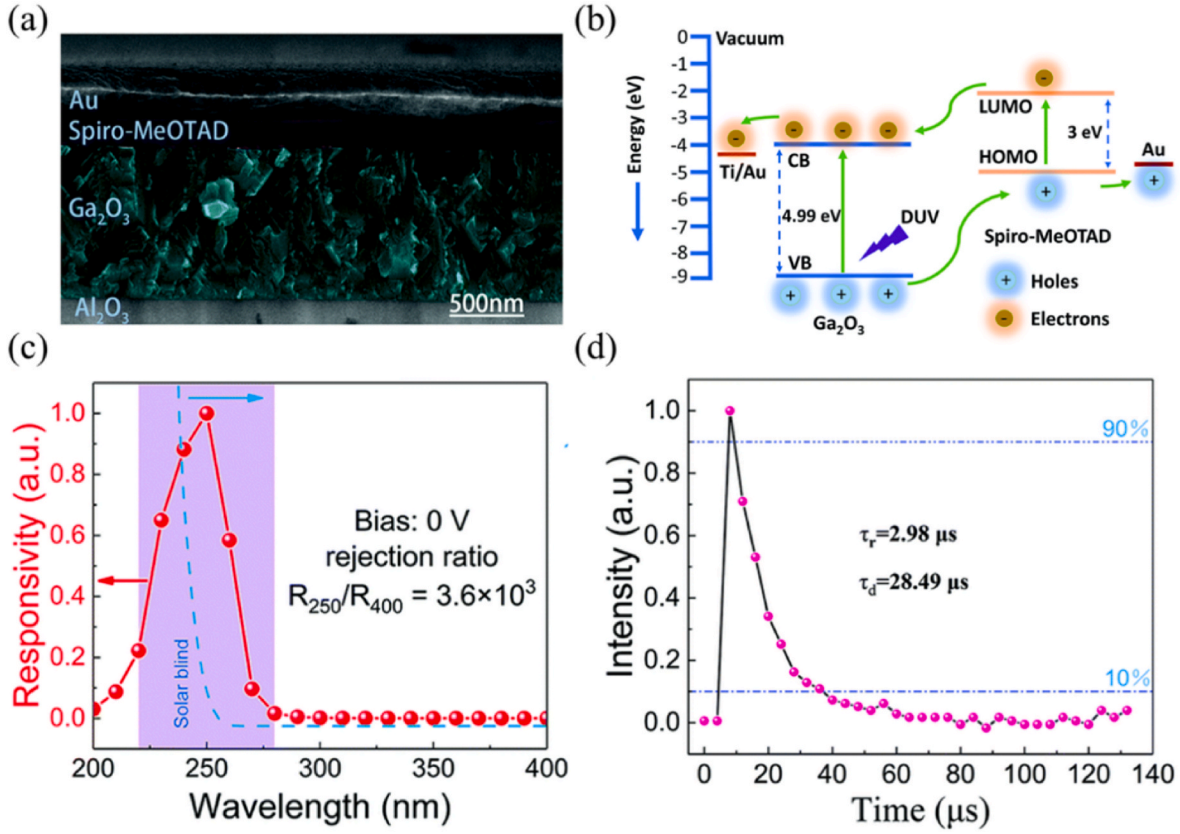

Fig. 20. (a) Cross-section SEM image of the Ga_2O_3/Spiro-MeOTAD photodetector. (b) Energy band diagram of Ga_2O_3/Spiro-MeOTAD photodetector. (c) Spectral responsivity with the corresponding absorption spectrum of the photodetector. (d) The time response of the photodetector under the 248 nm pulse laser without bias [145].

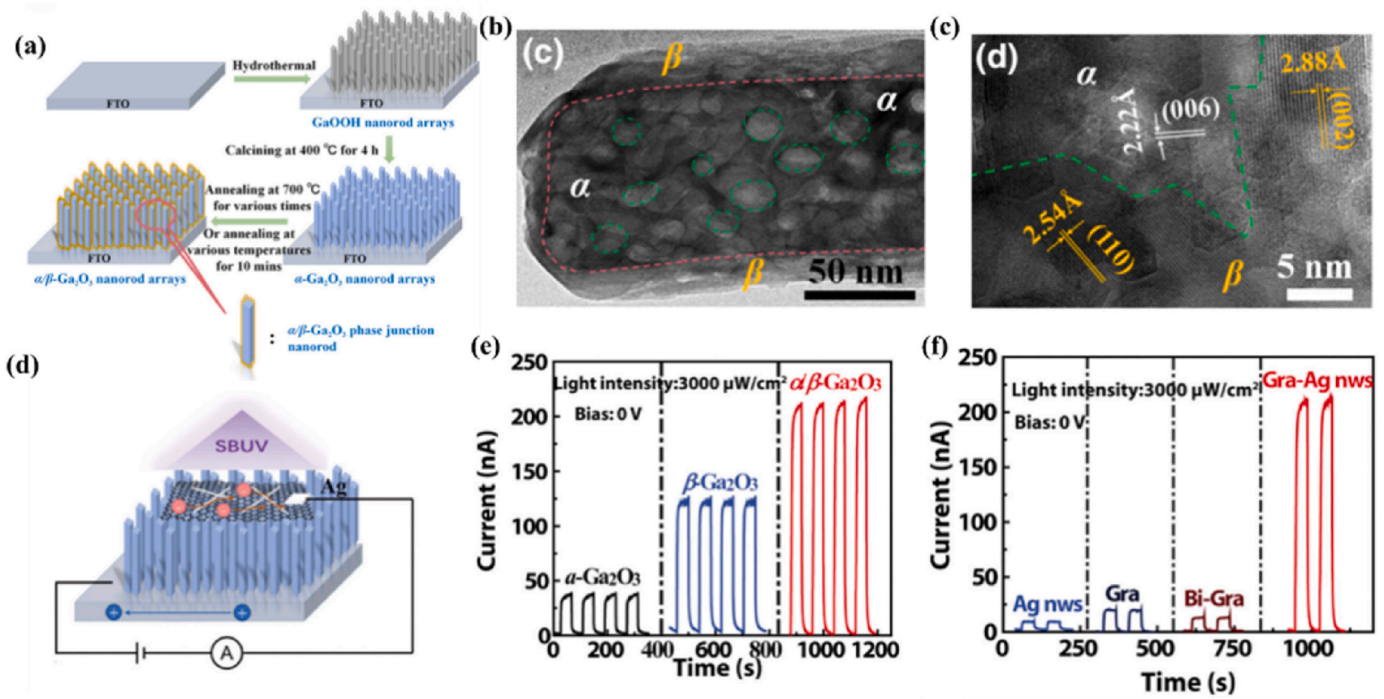

Fig. 21. (a) Schematic diagrams of preparation process of α/β-Ga_2O_3 phase junction NRAs. (b) TEM and (c) HRTEM image of α/β-Ga_2O_3 phase junction NRAs [147]. (d) Schematic diagram of the α/β-Ga_2O_3 phase junction NRAs photodetector. (e) *I-t* curves of α-Ga_2O_3, β-Ga_2O_3 and α/β-Ga_2O_3 photodetectors under 0 V. (f) *I-t* curves of α/β-Ga_2O_3 photodetectors with different top electrodes under 0 V [148].

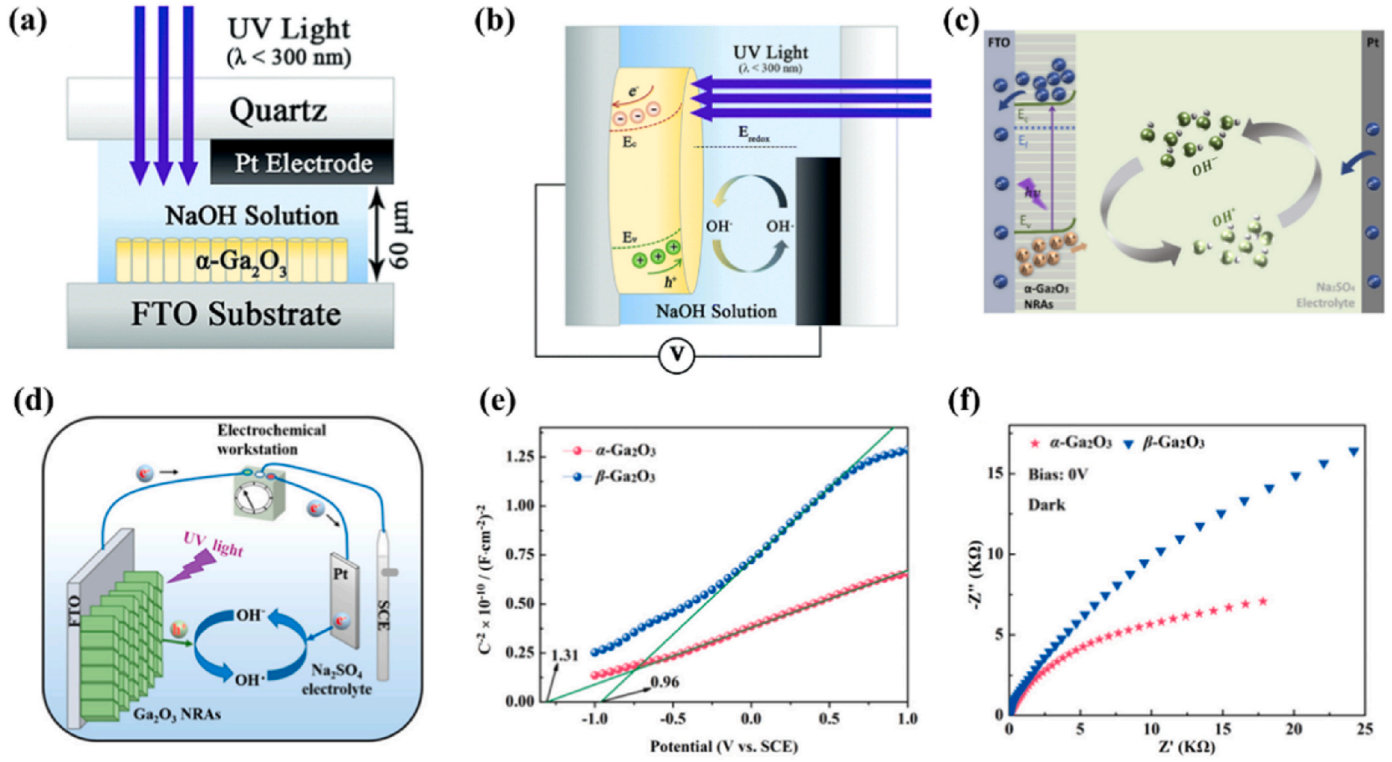

Fig. 22. (a) Schematic diagrams of the α-Ga_2O_3 PEC photodetector. (b) Working principle for the improved structured PEC UV detector under 0 V bias [149]. (c) Mechanism diagram of PEC self-powered ultraviolet photodetector based on α-Ga_2O_3 nanorod arrays [150]. (d) Structural diagram of Ga_2O_3 NRAs PEC photodetectors. (e) M − S and (f) EIS plots of α-Ga_2O_3 and β-Ga_2O_3 NRAs. [151].

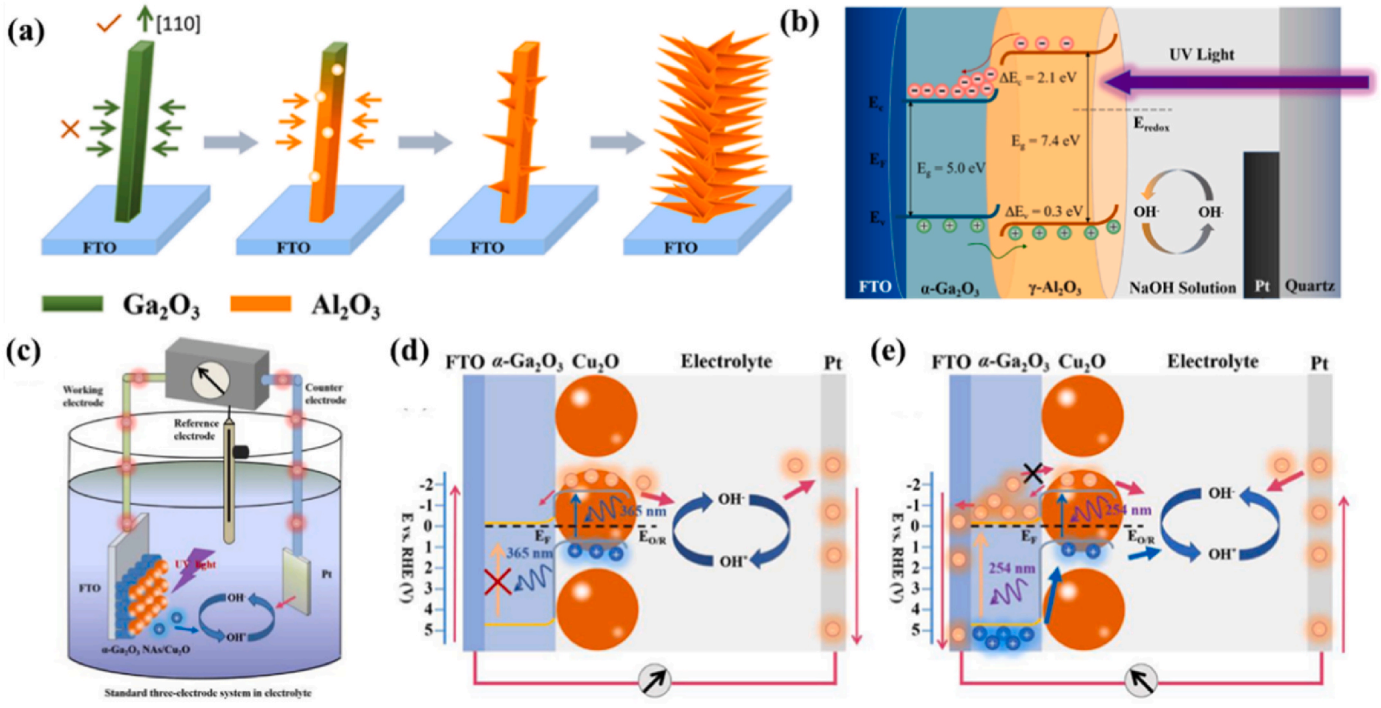

Fig. 23. (a) Schematic diagram for the formation of the tree-like branched structure. (b) Working schematic diagram of the PEC photodetector based on the α-Ga_2O_3-γ-Al_2O_3 [152]. (c) Schematic diagrams of the α-Ga_2O_3/Cu_2O PEC photodetector. (d) and (e) Schematic diagram of the α-Ga_2O_3/Cu_2O PEC photodetector [153].

research interest worldwide. Up to now, most of the reported Ga_2O_3 based self-powered photodetectors have been designed by utilizing the photovoltaic effect and can be divided into Schottky junction, heterojunction, phase junction, and PEC. Table 2 summarizes the parameters of self-powered solar-blind photodetectors based on Ga_2O_3. The metal-semiconductor Schottky junction photodetector composed of Ni/Au/β-Ga_2O_3 Schottky junction shows the highest photoresponsivity (9.78 A/W) at zero bias, followed by GaN/Sn: Ga_2O_3 heterojunction

Table 2
Parameter list of Ga_2O_3-based self-powered solar-blind photodetectors.

Type	Materials	PDCR	Responsivity (mA/W)	Rejection ratio	Detectivity (Jones)	Response speed	Ref
Schottky Junction	Au/β-Ga_2O_3	\	0.01	R_{258}/R_{280} ~ 11 R_{258}/R_{400} ~ 38	\	\	[47]
	Au/β-Ga_2O_3		\	R_{241}/R_{280} ~ 280 R_{241}/R_{400} ~ 1080	\	\	[48]
	Pt/Ge:β-Ga_2O_3	\	0.09	R_{230}/R_{350} ~ 10^4	\	\	[49]
	Ni/Au/β-Ga_2O_3	~ 10^3	1.4	\	\	1.1/0.3 s	[50]
	Au/Ga_2O_3/Si	~ 10^3	\	\	\	32.2/78 ms	[51]
	Ni/Au/β-Ga_2O_3	\	9.78×10^3	R_{212}/R_{350} ~ 10^4	3.92×10^{14}	5.19 μs	[52]
	LIG/Ga_2O_3	200	\	\	\	\	[53]
	Grahene/Sn:β-Ga_2O_3	\	\	\	\	0.62/0.67 s	[57]
	Grahene/β-Ga_2O_3	\	10.3	R_{235}/R_{400} ~ 228	\	2.24 μs	[58]
Hetero-junction	NSTO/Ga_2O_3	20	2.6	\	\	0.21\0.07 s	[65]
	Diamond/Ga_2O_3	37	0.2	R_{244}/R_{400} ~ 135	6.9×10^9	\	[66]
	MoS_2/Ga_2O_3	670	2.05	R_{254}/R_{400} ~ 1.6×10^3	1.21×10^{11}		[74]
	GaSe/Ga_2O_3	\	0.19	\	2.52×10^{14}	0.32/5.26 μs	[75]
	ZnO/Ga_2O_3 core-shell	\	9.7	R_{251}/R_{400} ~ 6.9×10^2	6.29×10^{12}	100/900 μs	[76]
	ZnO/Ga_2O_3	14.8	\	\	\	\	[77]
	Ga:ZnO/Ga_2O_3	127	0.763	\	\	0.179/0.272 s	[78]
	GaN/Ga_2O_3	74	28.44	\	\	0.14/0.07 s	[82]
	GaN/Sn:Ga_2O_3	6.1×10^4	3.05×10^3	R_{254}/R_{400} ~ 6×10^3	1.69×10^{13}	0.018 s	[83]
	CuSCN/Ga_2O_3	\	98×10^{-3}	\	9.7×10^{10}	\	[92]
	CuI/Ga_2O_3	\	2.49	\	\	\	[95]
	CuI/Ga_2O_3 core-shell	4×10^3	8.46	R_{200}/R_{600} ~ 8.8×10^3	7.75×10^{11}	97.8/28.9 ms	[96]
	$CuGaO_2$/Ga_2O_3	2.3×10^4	0.025	R_{254}/R_{365} ~ 2.0×10^4	0.9×10^{11}	0.26/0.14 s	[108]
	$CuCrO_2$/Ga_2O_3	3.5×10^4	0.12	R_{254}/R_{365} ~ 2.8×10^4	4.6×10^{11}	0.35/0.06 s	[108]
	NiO/Ga_2O_3	122	0.057	\	5.45×10^9	0.34/3.65 s	[114]
	NiO/Ga_2O_3	~ 100	0.245	\	0.189×10^9	12/8 ms	[115]
	Pt NPs/NiO/Ga_2O_3	~ 1000	4.27	\	4.2×10^9	4.6/7.6 ms	[115]
	VO_x/Ga_2O_3	1.1×10^8	28.91	R_{254}/R_{365} ~ 3.1×10^4	1.1×10^{14}	0.05/0.07 s	[116]
	$SnSrO_3$/Ga_2O_3	1.7×10^4	\	R_{254}/R_{365} ~ 2.1×10^3	1.3×10^{13}	0.15/0.06 s	[117]
	PEDOT:PSS/Ga_2O_3	\	29	R_{255}/R_{405} ~ 450	\	0.06/0.088 s	[135]
	PEDOT:PSS/Ga_2O_3	~ 10^4	2.6	R_{254}/R_{450} ~ 9×10^4	2.2×10^{13}	0.34/3 ms	[136]
	PEDOT:PSS/Ga_2O_3	\	37.4	/	9.2×10^{12}	3.31/71.2 μs	[137]
	Spiro-OMETAD/Ga_2O_3	~ 10^5	65	R_{250}/R_{400} ~ 3.6×10^3	3.95×10^{11}	2.98/28.49 μs	[145]
	TAPC/β-Ga_2O_3	5.9×10^5	1.41	/	10.2×10^{12}	0.27/0.05 s	[146]
Phase junction	α/β-Ga_2O_3	127	0.26	R_{254}/R_{365} ~ 2.7×10^3	2.8×10^9	0.54/1.63 s	[148]
PEC	α-Ga_2O_3 NRAs	/	0.21	R_{260}/R_{400} ~ 33.74	/	0.076/0.056 s	[149]
	α-Ga_2O_3 NRAs	1011	11.34	R_{254}/R_{365} ~ 207	2.68×10^{11}	1.51/0.18 s	[150]
	α-Ga_2O_3 NRAs	6.19	1.44	/	/	0.43/0.17 s	[151]
	β-Ga_2O_3 NRAs	28.97	3.81	/	/	0.29/0.16 s	[151]
	α-Ga_2O_3/γ-Ga_2O_3	51.3	0.17	R_{260}/R_{400} ~ 34.8	/	0.1/0.1 s	[152]
	α-Ga_2O_3/Cu_2O	/	0.42	/	/	10.3/10.1 s	[153]

photodetector (3.05 A/W). Compared with Schottky junction photodetector, the photodetectors based on heterojunction tend to have a lower dark current and a higher PDCR [such as GaN/Sn: Ga_2O_3 (6.1×10^4), $CuCrO_2/Ga_2O_3$ (3.5×10^4) and $CuGaO_2/Ga_2O_3$ (2.3×10^4)]. The devices based on both heterojunction and Schottky junction show fast photoresponse speed. While the photodetector based on graphene/Ga_2O_3 Schottky junction exhibits the quickest response speed (2.24 μs), followed by Au/β-Ga_2O_3 Schottky junction (5.19 μs), Spiro-OMETAD/Ga_2O_3 (2.98/28.49 μs) and PEDOT: PSS/Ga_2O_3 (3.3/71.2 μs). In general, heterojunction-type photodetectors exhibit higher optoelectronic performance (for example, high responsivity, high detectivity, and fast response time). However, some heterojunction photodetectors respond to UVB or UVA bands, while the other devices exhibit good spectral selectivity.

Although the photodetectors in the reported literature exhibit good solar-blind photoresponse performance, many challenges still need to be solved to commercialize. (1) P-type doping in Ga_2O_3 is still difficult, and homojunction pn type photodetector cannot be formed. Fortunately, Fang et al. recently grew a high-quality p-type N-doped β-Ga_2O_3 film. This novel p-type Ga_2O_3 film growth technique opens a new way to form Ga_2O_3 homojunction self-powered photodetectors. (2) More work must be done to enhance the response speed. Though the Ga_2O_3 based self-powered solar-blind photodetectors have comparable responsivity and specific detectivity performance compared with the commercial UV-enhanced Si photodiodes, the response speed is hard to meet practical demand. Currently, the fastest response speed of the reported Ga_2O_3 based self-powered solar-blind photodetectors is about 2 μs, while the faster response speeds, down to ns or ps, are desired. Hence, more effects must be done to enhance the response speed. (3) The weak light detection ability of the photodetectors needs to be further enhanced. The ability to detect weak signals determines the application of Ga_2O_3 based photodetectors. (4) Novel strategies should be developed to remarkably reduce the size and weight of self-powered photodetectors. A flexible device is also desired for some particular applications. However, up to now, there are few reports on self-powered flexible devices. We look forward to novel constructions and techniques to realize Ga_2O_3-based self-powered flexible devices. It is expected that more achievements in the Ga_2O_3 solar-blind DUV photodetection field will be attained to meet the huge demands of various applications.

Declaration of competing interest

The authors declare that they have no known competing financial interests or personal relationships that could have appeared to influence the work reported in this paper.

Data availability

Data will be made available on request.

Acknowledgements

This work was supported by the National Natural Science Foundation of China (No. 62274148).

References

[1] M. Razeghi, A. Rogalski, J. Appl. Phys. 79 (10) (1996) 7433–7473.
[2] H. Chen, K. Liu, L. Hu, A.A. Al-Ghamdi, X. Fang, Mater. Today 18 (9) (2015) 493–502.
[3] M. Razeghi, Proc. IEEE 90 (2002) 1006.
[4] M. Razeghi, IEEE Photon. J. 3 (2) (2011) 263–267.
[5] D. Kaur, M. Kumar, Adv. Opt. Mater. 9 (9) (2021): 2002160.
[6] X.H. Hou, Y.N. Zou, M.F. Ding, Y. Qin, Z.F. Zhang, X.L. Ma, P.J. Tan, S.J. Yu, X. Z. Zhou, X.L. Zhao, G.W. Xu, H.D. Sun, S.B. Long, J. Phys. D Appl. Phys. 54 (2021): 043001.
[7] X.L. Zhao, M.F. Ding, H.D. Sun, S.B. Long, Semiconduct. Semimet. 107 (2021) 101–141.
[8] B.R. Roy, V.G. Hill, E.F. Osborn, J. Am. Chem. Soc. 74 (1952) 719.
[9] D. Shinohara, S. Fujita, Jpn. J. Appl. Phys. 47 (9) (2008) 7311–7313.
[10] S. Fujita, K. Kaneko, J. Cryst. Growth 401 (2014) 588–592.
[11] K. Kaneko, T. Nomura, I. Kakeya, S. Fujita, Appl. Phys. Express 2 (2009): 075511.
[12] S.-D. Lee, K. Akaiwa, S. Fujita, Phys. Status Solidi C 10 (11) (2013) 1592–1595.
[13] S.-D. Lee, Y. Ito, K. Kaneko, S. Fujita, Jpn. J. Appl. Phys. 54 (3) (2015): 030301.
[14] R. Schewski, G. Wagner, M. Baldini, D. Gogova, Z. Galazka, T. Schulz, T. Remmele, T. Markurt, H. von Wenckstern, M. Grundmann, O. Bierwagen, P. Vogt, M. Albrecht, Appl. Phys. Express 8 (1) (2015): 011101.
[15] Y. Aoki, C. Wiemann, V. Feyer, H.S. Kim, C.M. Schneider, H. Ill-Yoo, M. Martin, Nat. Commun. 5 (2014) 3473.
[16] V.M. Bermudez, Chem. Phys. 323 (2–3) (2006) 193–203.
[17] M. Yamaga, E.G. Víllora, K. Shimamura, N. Ichinose, M. Honda, Phys. Rev. B 68 (15) (2003): 155207.
[18] T. Zacherle, P.C. Schmidt, M. Martin, Phys. Rev. B 87 (23) (2013): 235206.
[19] M. Orita, H. Hiramatsu, M.H. Ohta, M. Hirano, H. Hosono, Thin Solid Films 411 (2002) 134–139.
[20] R. Lorenzi, A. Paleari, N.V. Golubev, E.S. Ignat'eva, V.N. Sigaev, M. Niederberger, A. Lauria, J. Mater. Chem. C 3 (1) (2015) 41–45.
[21] M. Mitome, S. Kohiki, T. Nagai, K. Kurashima, K. Kimoto, Y. Bando, Cryst. Growth Des. 13 (8) (2013) 3577–3581.
[22] H.Y. Playford, A.C. Hannon, M.G. Tucker, D.M. Dawson, S.E. Ashbrook, R. J. Kastiban, J. Sloan, R.I. Walton, J. Phys. Chem. C 118 (29) (2014) 16188–16198.
[23] M. Takahashi, T. Nakatani, S. Iwamoto, T. Watanabe, M. Inoue, J. Phys-Condens. Mat. 18 (24) (2006) 5745–5757.
[24] W. Ting, S.S. Farvid, M. Abulikemu, P.V. Radovanovic, J. Am. Chem. Soc. 132 (2010) 9250–9252.
[25] S. Ge, Z. Zheng, Solid State Sci. 11 (2009) 1592–1596.
[26] Y. Oshima, E.G. Víllora, Y. Matsushita, S. Yamamoto, K. Shimamura, J. Appl. Phys. 118 (8) (2015): 085301.
[27] T. Harwing, F. Kellendonk, S. Slappendel, J. Phys. Chem. Solid. 39 (6) (1978) 675–680.
[28] P. Guo, J. Xiong, X. Zhao, T. Sheng, C. Yue, B. Tao, X. Liu, J. Mater. Sci. Mater. Electron. 25 (8) (2014) 3629–3632.
[29] H. He, R. Orlando, M.A. Blanco, R. Pandey, E. Amzallag, I. Baraille, M. Rérat, Phys. Rev. B 74 (19) (2006): 195123.
[30] J.B. Varley, J.R. Weber, A. Janotti, C.G. Van de Walle, Appl. Phys. Lett. 97 (2010): 142106.
[31] H. Peelaers, C.G. Van de Walle, Phys. Status Solidi B 252 (4) (2015) 828–832.
[32] K. Balakrishnan, A. Bandoh, M. Iwaya, S. Kamiyama, H. Amano, Isamu Akasaki, Jpn. J. Appl. Phys. 46 (2007) L307.
[33] M. Imura, K. Nakano, N. Fujimoto, N. Okada, K. Balakrishnan, M. Iwaya, S. Kamiyama, H. Amano, I. Akasaki, T. Noro, T. Takagi, A. Bandoh, Jpn. J. Appl. Phys. 45 (2006) 8639–8643.
[34] W. Yang, S.S. Hullavarad, B. Nagaraj, I. Takeuchi, R.P. Sharma, T. Venkatesan, R. D. Vispute, H. Shen, Appl. Phys. Lett. 82 (20) (2003) 3424–3426.
[35] G. Horowitz, Adv. Polym. Sci. 223 (2010) 113–153.
[36] R. Hackam, P. Harrop, IEEE Trans. Electron. Dev. 19 (1972) 1231–1238.
[37] S. Müller, H. von Wenckstern, F. Schmidt, D. Splith, F.-L. Schein, H. Frenzel, M. Grundmann, Appl. Phys. Express 8 (12) (2015): 121102.
[38] C.R. Crowell, S.M. Sze, Solid State Electron. 9 (1966) 1035–1048.
[39] A.M. Cowley, S.M. Sze, J. Appl. Phys. 36 (10) (1965) 3212–3220.
[40] C.Y. Wu, J. Appl. Phys. 53 (8) (1982) 5947–5950.
[41] Z. Zheng, X. Zu, Y. Zhang, W. Zhou, Mater. Today Phys. 15 (2020): 100262.
[42] K. Afroz, M. Moniruddin, N. Bakranov, N. Nuraje, J. Mater. Chem. 6 (2018) 21696–21718.
[43] H. Kroemer, Rev. Mod. Phys. 73 (2001) 783–793.
[44] X. Chen, F. Ren, S. Gu, J. Ye, Photon. Res. 7 (4) (2019) 381.
[45] L.X. Su, W. Yang, J. Cai, H.Y. Chen, X.S. Fang, Small 13 (2017): 1701687.
[46] G. Konstantatos, E.H. Sargent, Nat. Nanotechnol. 5 (6) (2010) 391–400.
[47] X. Chen, K. Liu, Z. Zhang, C. Wang, B. Li, H. Zhao, D. Zhao, D. Shen, ACS Appl. Mater. Interfaces 8 (6) (2016) 4185–4191.
[48] C. Yang, H. Liang, Z. Zhang, X. Xia, P. Tao, Y. Chen, H. Zhang, R. Shen, Y. Luo, G. Du, RSC Adv. 8 (12) (2018) 6341–6345.
[49] F. Alema, B. Hertog, A. Osinsky, P. Mukhopadhyay, M. Toporkov, W. V. Schoenfeld, E. Ahmadi, J. Speck, Proc. SPIE 10105, Oxide-Based Materials and Devices VIII, 2017, p. 101051M.
[50] A.S. Pratiyush, S. Krishnamoorthy, S. Kumar, Z. Xia, R. Muralidharan, S. Rajan, D. N. Nath, Jpn. J. Appl. Phys. 57 (6) (2018): 060313.
[51] K. Arora, N. Goel, M. Kumar, M. Kumar, ACS Photonics 5 (6) (2018) 2391–2401.
[52] Y. Xu, X. Chen, Y.F. Zhang, F.F. Ren, S.L. Gu, J.D. Ye, IEEE Electron. Device Lett. 41 (7) (2020) 997–1000.
[53] C. Wu, F.M. Wu, H.Z. Hu, C.Q. Ma, J.H. Ye, A.P. Liu, S.L. Wang, H.P. Wu, J. B. Wang, D.Y. Guo, Appl. Phys. Lett. 120 (10) (2022): 101102.
[54] C. Lee, X. Wei, J.W. Kysar, J. Hone, Science 321 (5887) (2008) 385–388.
[55] B. Chen, H. Huang, X. Ma, L. Huang, Z. Zhang, L.M. Peng, Nanoscale 6 (24) (2014) 15255–15261.
[56] X.-W. Fu, Z.-M. Liao, Y.-B. Zhou, H.-C. Wu, Y.-Q. Bie, J. Xu, D.-P. Yu, Appl. Phys. Lett. 100 (22) (2012): 223114.
[57] G. Kalita, R.D. Mahyavanshi, P. Desai, A.K. Ranade, M. Kondo, T. Dewa, M. Tanemura, Phys. Status Solidi-R. 12 (8) (2018): 1800198.
[58] M. Chen, J. Ma, P. Li, H. Xu, Y. Liu, Opt Express 27 (6) (2019) 8717–8726.
[59] M. Ai, D. Guo, Y. Qu, W. Cui, Z. Wu, P. Li, L. Li, W. Tang, J. Alloys Compd. 692 (2017) 634–638.
[60] W.Y. Kong, G.A. Wu, K.Y. Wang, T.F. Zhang, Y.F. Zou, D.D. Wang, L.B. Luo, Adv. Mater. 28 (48) (2016) 10725–10731.
[61] Y. Wang, Z. Yang, H. Li, S. Li, Y. Zhi, Z. Yan, X. Huang, X. Wei, W. Tang, Z. Wu, ACS Appl. Mater. Interfaces 12 (42) (2020) 47714–47720.
[62] H. Yang, H.M. Luo, H. Wang, I.O. Usov, N.A. Suvorova, M. Jain, D.M. Feldmann, P.C. Dowden, R.F. DePaula, Q.X. Jia, Appl. Phys. Lett. 92 (10) (2008): 102113.
[63] C.H. Jia, X.W. Sun, G.Q. Li, Y.H. Chen, W.F. Zhang, Appl. Phys. Lett. 104 (4) (2014): 043501.
[64] L. Wei, G.Q. Li, W.F. Zhang, J. Phys. D Appl. Phys. 49 (4) (2016): 045101.
[65] D. Guo, H. Liu, P. Li, Z. Wu, S. Wang, C. Cui, C. Li, W. Tang, ACS Appl. Mater. Interfaces 9 (2) (2017) 1619–1628.
[66] Y.-C. Chen, Y.-J. Lu, C.-N. Lin, Y.-Z. Tian, C.-J. Gao, L. Dong, C.-X. Shan, J. Mater. Chem. C 6 (21) (2018) 5727–5732.
[67] F. Yan, Z. Wei, X. Wei, Q. Lv, W. Zhu, K. Wang, Small Methods 2 (5) (2018): 1700349.
[68] L. Zeng, S. Lin, Z. Lou, H. Yuan, H. Long, Y. Li, W. Lu, S.P. Lau, D. Wu, Y.H. Tsang, NPG Asia Mater. 10 (4) (2018) 352–362.
[69] X. Zhang, H. Cheng, H. Zhang, Adv. Mater. 29 (35) (2017): 1701704.
[70] Y. Wang, X. Huang, D. Wu, R. Zhuo, E. Wu, C. Jia, Z. Shi, T. Xu, Y. Tian, X. Li, J. Mater. Chem. C 6 (18) (2018) 4861–4865.
[71] D. Wu, Z. Lou, Y. Wang, Z. Yao, T. Xu, Z. Shi, J. Xu, Y. Tian, X. Li, Y.H. Tsang, Sol. Energ. Mat. Sol. C. 182 (2018) 272–280.
[72] R. Zhuo, Y. Wang, D. Wu, Z. Lou, Z. Shi, T. Xu, J. Xu, Y. Tian, X. Li, J. Mater. Chem. C 6 (2) (2018) 299–303.
[73] Z. Lou, L. Zeng, Y. Wang, D. Wu, T. Xu, Z. Shi, Y. Tian, X. Li, Y.H. Tsang, Opt. Lett. 42 (17) (2017) 3335–3338.
[74] R. Zhuo, D. Wu, Y. Wang, E. Wu, C. Jia, Z. Shi, T. Xu, Y. Tian, X. Li, J. Mater. Chem. C 6 (41) (2018) 10982–10986.
[75] Y.H. Wang, Y.Q. Tang, H.R. Li, Z.B. Yang, Q.Y. Zhang, Z.B. He, X. Huang, X. H. Wei, W.H. Tang, W. Huang, Z.P. Wu, ACS Photonics 8 (2021) 2256–2264.
[76] B. Zhao, F. Wang, H. Chen, L. Zheng, L. Su, D. Zhao, X. Fang, Adv. Funct. Mater. 27 (17) (2017): 1700264.
[77] D.Y. Guo, H.Z. Shi, Y.P. Qian, M. Lv, P.G. Li, Y.L. Su, Q. Liu, K. Chen, S.L. Wang, C. Cui, C.R. Li, W.H. Tang, Semicond. Sci. Technol. 32 (3) (2017): 03LT01.
[78] L. Wu, X. Jiao, D. Wang, W. Guo, L. Li, F.Huang Li, W. Tang, J. Mater. Chem. C 5 (34) (2017) 8688–8693.
[79] N. Aggarwal, S.T.C. Krishna, L. Goswami, M. Mishra, G. Gupta, K.K. Maurya, S. Singh, N. Dilawar, M. Kaur, Cryst. Growth Des. 15 (5) (2015) 2144–2150.
[80] S. Krishna, N. Aggarwal, M. Mishra, K.K. Maurya, S. Singh, N. Dilawar, S. Nagarajan, G. Gupta, Phys. Chem. Chem. Phys. 18 (11) (2016) 8005–8014.
[81] J. Montes, C. Yang, H. Fu, T.-H. Yang, K. Fu, H. Chen, J. Zhou, X. Huang, Y. Zhao, Appl. Phys. Lett. 114 (16) (2019): 162103.
[82] P. Li, H. Shi, K. Chen, D. Guo, W. Cui, Y. Zhi, S. Wang, Z. Wu, Z. Chen, W. Tang, J. Mater. Chem. C 5 (40) (2017) 10562–10570.
[83] D. Guo, Y. Su, H. Shi, P. Li, N. Zhao, J. Ye, S. Wang, A. Liu, Z. Chen, C. Li, W. Tang, ACS Nano 12 (12) (2018) 12827–12835.
[84] D. Aldakov, C. Chappaz-Gillot, R. Salazar, V. Delaye, K.A. Welsby, V. Ivanova, P. R. Dunstan, J. Phys. Chem. C 118 (29) (2014) 16095–16103.
[85] S.M. Hatch, J. Briscoe, S. Dunn, Adv. Mater. 25 (6) (2013) 867–871.
[86] K. Khojier, H. Savaloni, Z. Sadeghi, J. Theor. Appl. Phys. 8 (1) (2014) 116.
[87] P. Pattanasattayavong, A.D. Mottram, F. Yan, T.D. Anthopoulos, Adv. Funct. Mater. 25 (43) (2015) 6802–6813.
[88] L. Tsetseris, Phys. Chem. Chem. Phys. 18 (11) (2016) 7837–7840.
[89] N. Wijeyasinghe, T.D. Anthopoulos, Semicond. Sci. Technol. 30 (10) (2015): 104002.
[90] N. Wijeyasinghe, F. Eisner, L. Tsetseris, Y.-H. Lin, A. Seitkhan, J. Li, F. Yan, O. Solomeshch, N. Tessler, P. Patsalas, T.D. Anthopoulos, Adv. Funct. Mater. 28 (31) (2018): 1802055.
[91] N. Wijeyasinghe, A. Regoutz, F. Eisner, T. Du, L. Tsetseris, Y.-H. Lin, H. Faber, P. Pattanasattayavong, J. Li, F. Yan, M.A. McLachlan, D.J. Payne, M. Heeney, T. D. Anthopoulos, Adv. Funct. Mater. 27 (35) (2017): 1701818.
[92] S. Li, D. Guo, P. Li, X. Wang, Y. Wang, Z. Yan, Z. Liu, Y. Zhi, Y. Huang, Z. Wu, W. Tang, ACS Appl. Mater. Interfaces 11 (38) (2019) 35105–35114.
[93] A. Liu, H. Zhu, W.T. Park, S.J. Kang, Y. Xu, M.G. Kim, Y.Y. Noh, Adv. Mater. 30 (2018): 1802379.

[94] Y. Zhang, S. Li, W. Yang, M.K. Joshi, X. Fang, J. Phys. Chem. Lett. 10 (10) (2019) 2400–2407.
[95] M.E. Ayhan, M. Shinde, B. Todankar, P. Desai, A.K. Ranade, M. Tanemura, G. Kalita, Mater. Lett. 262 (2020): 127074.
[96] S. Li, Y. Zhi, C. Lu, C. Wu, Z. Yan, Z. Liu, J. Yang, X. Chu, D. Guo, P. Li, Z. Wu, W. Tang, J. Phys. Chem. Lett. 12 (2021) 447–453.
[97] S. Dursun, I.C. Kaya, V. Kalem, H. Akyildiz, Dalton Trans. 47 (41) (2018) 14662–14678.
[98] M. Kumar, H. Zhao, C. Persson, Semicond. Sci. Technol. 28 (6) (2013): 065003.
[99] Y. Li, Y. Song, Y. Jiang, M. Hu, Z. Pan, X. Xu, H. Chen, Y. Li, L. Hu, X. Fang, Adv. Funct. Mater. 27 (23) (2017): 1701066.
[100] T. Omata, H. Nagatani, I. Suzuki, M. Kita, H. Yanagi, N. Ohashi, J. Am. Chem. Soc. 136 (9) (2014) 3378–3381.
[101] A. Renaud, L. Cario, P. Deniard, E. Gautron, X. Rocquefelte, Y. Pellegrin, E. Blart, F. Odobel, S. Jobic, J. Phys. Chem. C 118 (1) (2013) 54–59.
[102] L. Shi, F. Wang, Y. Wang, D. Wang, B. Zhao, L. Zhang, D. Zhao, D. Shen, Sci. Rep. 6 (2016): 21135.
[103] C.-Y. Tsay, C.-L. Chen, J. Cryst. Growth 468 (2017) 662–665.
[104] J. Wang, V. Ibarra, D. Barrera, L. Xu, Y.J. Lee, J.W. Hsu, J. Phys. Chem. Lett. 6 (6) (2015) 1071–1075.
[105] D. Xiong, H. Chang, Q. Zhang, S. Tian, B. Liu, X. Zhao, Appl. Surf. Sci. 347 (2015) 747–754.
[106] D. Xiong, Z. Xu, X. Zeng, W. Zhang, W. Chen, X. Xu, M. Wang, Y.-B. Cheng, J. Mater. Chem. 22 (47) (2012).
[107] Z. Xu, D. Xiong, H. Wang, W. Zhang, X. Zeng, L. Ming, W. Chen, X. Xu, J. Cui, M. Wang, S. Powar, U. Bach, Y.-B. Cheng, J. Mater. Chem. 2 (9) (2014) 2968–2976.
[108] C. Wu, L. Qiu, S. Li, D. Guo, P. Li, S. Wang, P. Du, Z. Chen, A. Liu, X. Wang, H. Wu, F. Wu, W. Tang, Mater. Today Phys. 17 (2021): 100335.
[109] A.A. Ahmed, N. Afzal, M. Devarajan, S. Subramani, Mater. Res. Express 3 (11) (2016): 116405.
[110] A. Hakim, J. Hossain, K.A. Khan, Renew. Energy 34 (12) (2009) 2625–2629.
[111] Y. Shen, X. Yan, Z. Bai, X. Zheng, Y. Sun, Y. Liu, P. Lin, X. Chen, Y. Zhang, RSC Adv. 5 (8) (2015) 5976–5981.
[112] C. Wei, J. Xu, S. Shi, R. Cao, J. Chen, H. Dong, X. Zhang, S. Yin, L. Li, J. Mater. Chem. C 7 (30) (2019) 9369–9379.
[113] X.H. Xia, J.P. Tu, J. Zhang, X.L. Wang, W.K. Zhang, H. Huang, Sol. Energ. Mater. Sol. C. 92 (6) (2008) 628–633.
[114] Y. Wang, C. Wu, D. Guo, P. Li, S. Wang, A. Liu, C. Li, F. Wu, W. Tang, ACS Appl. Electron. Mater. 2 (7) (2020) 2032–2038.
[115] J. Yu, M. Yu, Z. Wang, L. Yuan, Y. Huang, L. Zhang, Y. Zhang, R. Jia, IEEE Trans. Electron. Dev. 67 (8) (2020) 3199–3204.
[116] Z. Guo, D. Jiang, N. Hu, X. Yang, W. Zhang, Y. Duan, S. Gao, Q. Liang, T. Zheng, J. Lv, Nanoscale Res. Lett. 13 (1) (2018) 168.
[117] C. Jia, X. Li, N. Xin, Y. Gong, J. Guan, L. Meng, S. Meng, X. Guo, Adv. Energy Mater. 6 (17) (2016): 1600431.
[118] P. Joshna, S.R. Gollu, P.M.P. Raj, B. Rao, P. Sahatiya, S. Kundu, Nanotechnology 30 (36) (2019): 365201.
[119] N. Lu, Y. Gu, Y. Weng, Z. Da, Y. Ding, Mater. Res. Express 6 (9) (2019): 095033.
[120] S. Lia, J.Y. Yue, Z.Y. Yan, Z. Liu, C. Lu, P.G. Li, D.Y. Guo, Z.P. Wu, Y.F. Guo, W. H. Tang, J. Alloys Compd. 902 (2022): 163801.
[121] C. Wu, F.M. Wu, L.P. Deng, S. Li, S.L. Wang, L. Cheng, A.P. Liu, J.B. Wang, W. H. Tang, D.Y. Guo, Vacuum 201 (2022): 111064.
[122] H. Chen, P. Yu, Z. Zhang, F. Teng, L. Zheng, K. Hu, X. Fang, Small 12 (42) (2016) 5809–5816.
[123] O. Game, U. Singh, T. Kumari, A. Banpurkar, S. Ogale, Nanoscale 6 (1) (2014) 503–513.
[124] H.-G. Li, G. Wu, M.-M. Shi, L.-G. Yang, H.-Z. Chen, M. Wang, Appl. Phys. Lett. 93 (15) (2008): 153309.
[125] P. Lin, X. Yan, Z. Zhang, Y. Shen, Y. Zhao, Z. Bai, Y. Zhang, ACS Appl. Mater. Interfaces 5 (9) (2013) 3671–3676.
[126] S. Mridha, D. Basak, Appl. Phys. Lett. 92 (14) (2008): 142111.
[127] D. Shao, M. Yu, H. Sun, G. Xin, J. Lian, S. Sawyer, ACS Appl. Mater. Interfaces 6 (16) (2014) 14690–14694.
[128] Y. Shen, X. Yan, H. Si, P. Lin, Y. Liu, Y. Sun, Y. Zhang, ACS Appl. Mater. Interfaces 8 (9) (2016) 6137–6143.
[129] S. Yang, J. Gong, Y. Deng, J. Mater. Chem. 22 (28) (2012): 13899.
[130] S. Yang, H. Yang, H. Ma, S. Guo, F. Cao, J. Gong, Y. Deng, Chem. Commun. 47 (9) (2011) 2619–2621.
[131] X. Zhang, J. Li, W. Yang, B. Leng, P. Niu, X. Jiang, B. Liu, ACS Appl. Mater. Interfaces 11 (27) (2019) 24459–24467.
[132] Y.F. Wang, L. Li, H.B. Wang, L.X. Su, H.Y. Chen, W.P. Bian, J.G. Ma, B.S. Li, Z. G. Liu, A.D. Shen, Nanoscale 12 (2020) 1406.
[133] J.P. Thomas, M.A. Rahman, S. Srivastava, J.S. Kang, D. McGillivray, M. Abd-Ellah, N.F. Heinig, K.T. Leung, ACS Nano 12 (9) (2018) 9495–9503.
[134] Q. Wei, M. Mukaida, Y. Naitoh, T. Ishida, Adv. Mater. 25 (20) (2013) 2831–2836.
[135] D. Zhang, W. Zheng, R. Lin, Y. Li, F. Huang, Adv. Funct. Mater. 29 (26) (2019): 1900935.
[136] H. Wang, H. Chen, L. Li, Y. Wang, L. Su, W. Bian, B. Li, X. Fang, J. Phys. Chem. Lett. 10 (21) (2019) 6850–6856.
[137] S. Li, Z. Yan, Z. Liu, J. Chen, Y. Zhi, D. Guo, P. Li, Z. Wu, W. Tang, J. Mater. Chem. C 8 (2020) 1292–1300.
[138] H. Bai, T. Shen, J. Tian, J. Mater. Chem. C 5 (40) (2017) 10543–10548.
[139] A. Bera, A. Das Mahapatra, S. Mondal, D. Basak, ACS Appl. Mater. Interfaces 8 (50) (2016) 34506–34512.
[140] F. Cao, L. Meng, M. Wang, W. Tian, L. Li, Adv. Mater. 31 (12) (2019): e1806725.
[141] Z. Hawash, L.K. Ono, Y. Qi, Adv. Mater. Inter. 5 (1) (2017): 1700623.
[142] G.-W. Kim, D.V. Shinde, T. Park, RSC Adv. 5 (120) (2015) 99356–99360.
[143] Y. Lin, G. Lin, B. Sun, X. Guo, Adv. Funct. Mater. 28 (7) (2018): 1705589.
[144] J. Wei, H. Li, Y. Zhao, W. Zhou, R. Fu, Y. Leprince-Wang, D. Yu, Q. Zhao, Nano Energy 26 (2016) 139–147.
[145] Z. Yan, S. Li, Z. Liu, Y. Zhi, J. Dai, X. Sun, S. Sun, D. Guo, X. Wang, P. Li, Z. Wu, L. Li, W. Tang, J. Mater. Chem. C 8 (13) (2020) 4502–4509.
[146] C. Wu, F. Wu, C. Ma, S. Li, A. Liu, X. Yang, Y. Chen, J. Wang, D. Guo, Mater. Today Phys. 23 (2022): 100643.
[147] D.Y. Guo, K. Chen, S.L. Wang, F.M. Wu, A.P. Liu, C.R. Li, P.G. Li, C.K. Tan, andW. H. Tang, Phys. Rev. Appl. 13 (2020): 024051.
[148] C. Wu, C. He, D. Guo, F. Zhang, P. Li, S. Wang, A. Liu, F. Wu, W. Tang, Mater. Today Phys. 12 (2020): 100193.
[149] J.H. Zhang, S.J. Jiao, D.B. Wang, S.M. Ni, S.Y. Gao, J.Z. Wang, J. Mater. Chem. C 7 (2019) 6867–6871.
[150] L.J. Huang, Z.R. Hu, X.W. He, T.Y. Ma, M.C. Li, H. Zhang, Y.Q. Xiong, C.Y. Kong, L.J. Ye, H.L. Li, W.J. Li, Opt. Mater. Express 11 (7) (2021) 2089–2098.
[151] K. Chen, S.L. Wang, C.R. He, H.W. Zhu, H.L. Zhao, D.Y. Guo, Z.W. Chen, J. Q. Shen, P.G. Li, A.P. Liu, C.R. Li, F.M. Wu, W.H. Tang, ACS Appl. Nano Mater. 2 (2019) 6169–6177.
[152] J.H. Zhang, S.J. Jiao, D.B. Wang, S.Y. Gao, J.Z. Wang, L.C. Zhao, Appl. Surf. Sci. 541 (2021): 148380.
[153] C.R. He, D.Y. Guo, K. Chen, S.L. Wang, J.Q. Shen, N. Zhao, A.P. Liu, Y.Y. Zheng, P. G. Li, Z.P. Wu, C.R. Li, F.M. Wu, Weihua Tang, ACS Appl. Nano Mater. 2 (2019) 4095–4103.
[154] W. Zheng, R.C. Lin, J.X. Ran, Z.J. Zhang, X. Ji, F. Huang, ACS Nano 12 (2018) 425–431.
[155] W. Zheng, L.M. Jia, F. Huang, iScience 23 (6) (2020): 101145.
[156] L.M. Jia, F. Huang, W. Zheng, Adv. Opt. Mater. 10 (8) (2022): 2102424.
[157] L.M. Jia, W. Zheng, F. Huang, PhotoniX 1 (2020) 22.
[158] Y.C. Chen, Y.J. Lu, X. Yang, S.F. Li, K.Y. Li, X.X. Chen, Z.Y. Xu, J.H. Zang, C. X. Shan, Mater. Today Phys. 18 (2021): 100369.
[159] H.W. Liu, S.R. Zhou, H. Zhang, L.J. Ye, Y.Q. Xiong, P. Yu, W.J. Li, X. Yang, H.L. Li, C.Y. Kong, J. Phys. D Appl. Phys. 55 (2022): 305104.
[160] S.R. Zhou, X. Peng, H.W. Liu, Z.F. Zhang, L.J. Ye, H.L. Li, Y.Q. Xiong, L.B. Niu, F. L. Chen, L. Fang, C.Y. Kong, W.J. Li, X. Yang, Hong Zhang, Opt. Mater. Express 12 (2022) 327.